Ore Geology Reviews 104 (2019) 462–476

Contents lists available at ScienceDirect

Ore Geology Reviews

journal homepage: www.elsevier.com/locate/oregeorev

Genesis of the Dongguashan skarn Cu-(Au) deposit in Tongling, Eastern China: Evidence from fluid inclusions and H-O-S-Pb isotopes

Zhong-fa Liu[a,b], Yong-jun Shao[a,b,*], Cheng Wang[a,b], Qing-quan Liu[a]

[a] Key Laboratory of Metallogenic Prediction of Nonferrous Metals and Geological Environment Monitoring (Central South University), Ministry of Education, Changsha 410083, China

[b] School of Geoscience and Info Physics, Central South University, Changsha 410083, China

ARTICLE INFO

Keywords:
Ore genesis
Fluid inclusions
H-O-S-Pb isotopes
Dongguashan
Eastern China

ABSTRACT

The Dongguashan copper-(gold) deposit is located in the Eastern Tongling ore district of the Middle-Lower Yangtze River Valley Metallogenic Belt (MLYRB), Eastern China. The Cu-(Au) mineralization is associated with the Qingshanjiao quartz monzodiorite and consists of various types including stratiform, porphyry, vein-like and skarn. There are three deposit models, including: 1) stratabound skarn-type; 2) exhalative sedimentary (SEDEX)-hydrothermal superimposition-type; and 3) exhalative sedimentary (SEDEX) type. The ore-forming processes can be divided into the prograde skarn alteration (Stage I), retrograde alteration (Stage II) and quartz-carbonate alteration (Stage III). Four types of fluid inclusions (FIs) are recognized at Dongguashan: Vapor-rich two-phase aqueous (Type I), liquid-rich two-phase aqueous (Type II), daughter-mineral-bearing three-phase (homogenized to liquid by the disappearance of vapor phase; Type III), and daughter-mineral-bearing three-phase (homogenized to liquid by the disappearance of daughter minerals; Type IV). All four types of FIs are present in Stage II. Stage I does not contain Type IV FIs, and only Type II FIs are found in Stage III. For Stage I, Type I, II and III FIs homogenized at 379–548 °C, 319–522 °C and 450–512 °C, respectively, with salinities of 10.1–19.6, 5.9–19.4 and 36.7–43.3 wt% NaCl equivalent. For Stage II, Type I, II, III and IV FIs homogenized at 286–378 °C, 235–372 °C, 265–349 °C and 324–350 °C, respectively, with salinities of 1.4–17.0, 4.3–16.1, 34.7–40.6 and 34.4–41.0 wt% NaCl equivalent. The Type I to III FIs in Stage I and II have similar homogenization temperatures but different salinities, which indicates the occurrence of fluid immiscibility. Hydrogen-oxygen isotopes of the quartz ($\delta D = -84.0$ to $-71.5‰$, $\delta^{18}O_{H2O} = +4.51$ to $+8.97‰$) and calcite ($\delta D = -70.7$ to $-60.95‰$, $\delta^{18}O_{H2O} = +4.41$ to $+4.91‰$) suggest that the ore-forming fluids were principally magmatic-derived. $\delta^{34}S$ values of the stratiform orebodies ($+4.1$ to $+5.3‰$), vein-like orebodies ($+4.2$ to $+5.7‰$), skarn orebodies ($+4.9‰$), porphyry orebodies ($+5.1$ to $+5.7‰$) and the Qingshanjiao pluton (-2.2 to $+5.2‰$) are different from those of the wall rocks (-29.5 to $-4.6‰$), suggesting that wall rocks were unlikely to be a major sulfur source. Lead isotopes of the sulfides from the different orebody types are similar to those of the plagioclase from the Mesozoic intermediate-felsic rocks in the MLYRB, suggesting that they have had similar Pb source. Sulfur and lead isotopes suggest that the ore-forming materials were derived from a deep-seated magmatic source. The ore-forming fluid immiscibility during Stage I and II may have altered the physicochemical conditions of the hydrothermal fluid system, leading to the Cu-(Au) sulfide precipitation. Based on the ore geological and alteration/mineralization features, mineral assemblages, ore-forming material source and fluid evolution, we consider that Dongguashan is best classified as a porphyry–skarn Cu-(Au) deposit.

1. Introduction

As one of the most important Cu-Fe-Au-Mo mineral provinces in Eastern China, the Middle-Lower Yangtze River Valley Metallogenic Belt (MLYRB) extends from Wuhan (Hubei Province) in the west to Zhenjiang (Jiangsu Province) in the east (Mao et al., 2011). It is bounded by the Xiangfan-Guangji fault (XGF) to the north, the Tanlu fault (TLF) to the northeast, and the Yangxing-Changzhou fault (YCF) to the south (Fig. 1; Chang et al., 1991; Zhai et al., 1992; Mao et al., 2011; Zhou et al., 2016). The crustal-scale Yangtze fault zone was likely

* Corresponding author at: Key Laboratory of Metallogenic Prediction of Nonferrous Metals and Geological Environment Monitoring (Central South University), Ministry of Education, Changsha 410083, China.
E-mail address: shaoyongjun@126.com (Y.-j. Shao).

https://doi.org/10.1016/j.oregeorev.2018.11.021
Received 10 January 2018; Received in revised form 31 October 2018; Accepted 20 November 2018
Available online 20 November 2018
0169-1368/

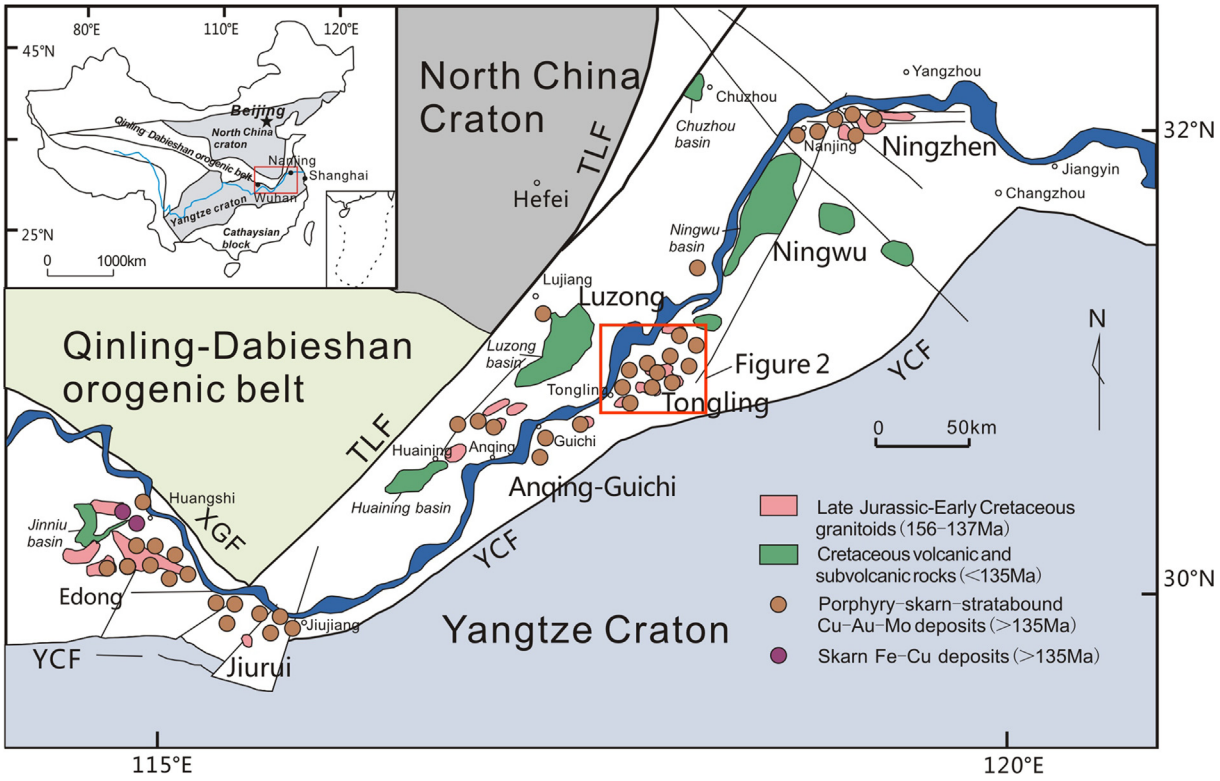

Fig. 1. Map showing the location of the Tongling ore district, and the major porphyry/skarn/stratabound Cu-Au-Mo (> 135 Ma) deposits along the Middle-Lower Yangtze River Valley Metallogenic Belt (MLYRB) (modified after Mao et al. (2011)). TLF-Tancheng-Lujiang fault, XGF-Xiangfan-Guangji fault, YCF-Yangxing-Changzhou fault.

developed since the Mesozoic (Chang et al., 1991). Prolonged and multiphase tectonothermal activities have developed several Cu-Fe-Au-Mo ore districts in the MLYRB (Zhou et al., 2008, 2016). From west to east, these ore districts include the Edong, Jiurui, Anqing-Guichi, Tongling, Luzong, Ningwu and Ningzhen (Chang et al., 1991; Mao et al., 2009, 2011; Zhou et al., 2008, 2016). Major deposits in the belt include Tonglushan in Edong, Chengmenshan in Jiuri, Anqing and Yueshan in Anqing, Dongguashan in Tongling, and Taocun in Ningwu (Fig. 1). Most of these deposits are porphyry-skarn Cu-Mo or Cu-Au deposits related to the Yanshanian (Jurassic-Cretaceous) magmatism. These deposits can be divided into two major types: 1) apatite-magnetite; and 2) porphyry-skarn-stratabound Cu-Au-Mo-Fe deposits (Zhai et al., 1996; Pan and Dong, 1999; Yu and Mao, 2002; Mao et al., 2006). The former is largely hosted in the Ningwu and Luzong ore districts and belongs to porphyry-type Fe deposits (Ningwu Research Group, 1978; Zhang, 1986). Yu and Mao (2002) considered that these deposits are similar to the Kiruna type. The presence of stratiform orebodies and evidence of syngenetic mineralization in many of these Cu-Au-Mo-Fe deposits have led to some suggestions that these deposits are Variscan (late Paleozoic) submarine exhalative sedimentary (SEDEX)-type overprinted by Yanshanian (Jurassic-Cretaceous) magmatic-hydrothermal processes (Zhou et al., 2000; Gu et al., 2007; Zeng et al., 2005; Lu et al., 2008; Liu et al., 2009; Guo et al., 2010, 2011; Hou et al., 2011; Jiang et al., 2011). However, some other authors (Chang et al., 1991; Pan and Dong, 1999; Mao et al., 2009, 2011; Xu et al., 2008a, 2010, 2014; Cao et al., 2017; Li et al., 2017, Li et al., 2018) considered that these deposits are skarn-type as most of the orebodies are closely related to the calc-/magnesian-skarn.

The Dongguashan Cu-(Au) deposit is located in the Tongling ore district. This deposit contains approximately 0.98 Mt Cu metal at 1.02 wt%, and 29 t Au at 0.26 g/t. This deposit has a distinct stratabound feature, and the major stratiform orebodies and skarn are hosted in the Carboniferous Huanglong and Chuanshan formations. These stratiform orebodies account for 98% of the total ore reserve at Dongguashan. The Dongguashan deposit is a representative of the stratiform deposits in the MLYRB, and its research would help to understand the origin and formation mechanism of this deposit type in the MLYRB.

The Dongguashan Cu-(Au) deposit was variably attributed to be: 1) stratabound skarn-type (Chang et al., 1991; Pan and Dong, 1999; Ling and Liu, 2003; Mao et al., 2009, 2011; Xu et al., 2014); 2) exhalative sedimentary (SEDEX)-hydrothermal overprinting-type (Gu et al., 2007; Zhou et al., 2000; Zeng et al., 2005; Zaw et al., 2007; Lu et al., 2008; Guo et al., 2010, 2011; Hou et al., 2011; Jiang et al., 2011; Liu et al., 2009; Cao et al., 2016); and 3) exhalative sedimentary (SEDEX) type (Gu et al., 2002; Xu et al., 2004a; Xu et al., 2004b; Li et al., 2006; Wang et al., 2007). Publications on fluid inclusions (FIs) from Dongguashan are scarce (Ling and Liu, 2002; Xu et al., 2005), there is no systematic study on the FI temperature and salinity. Up till now, the sources of metals and ore-forming fluids, fluid evolution, and the ore-precipitation mechanism at Dongguashan remain poorly constrained, and systematic isotopic comparison of the different types of ores, intrusions and surrounding rocks are lacking.

In this paper, we present new data on H-O-S-Pb isotopes and fluid inclusions from Dongguashan, and discuss the possible source of metals and the characteristics and evolution of the ore-forming fluids. With these new data, we propose an ore genetic model for the Dongguashan Cu-(Au) deposit.

2. Regional geological setting

The Tongling ore district is located in the middle part of the MLYRB and the northeastern margin of the Yangtze craton (part of the South China block) (Chang et al., 1991; Tang et al., 1998). The district comprises several ore fields, such as (from west to east) the Tongguanshan, Shizishan, Xinqiao, Fenghuangshan and Shatanjiao. Tectonic

evolution of the Tongling region is divided into three main stages: 1) formation of the pre-Sinian (late Neoproterozoic) basement; 2) deposition of the Sinian to Early Triassic sedimentary cover; and 3) Middle Triassic to Cenozoic intraplate deformation (Ma and Ge, 1989; Chang et al., 1991; Zhai et al., 1992; Liu et al., 1996).

Outcropping sequences in the Tongling ore district comprise mainly Silurian fine sandstone and shale, Devonian quartz sandstone and shale, Carboniferous limestone, Lower Permian carbonate rocks, Upper Permian sandstone and shale, Lower-Middle Triassic carbonate rocks and sandstone, and Jurassic-Cretaceous sandstone and shale. The Cu-(Au) orebodies are located mainly in neritic- and littoral-facies carbonate sequences, e.g., the Carboniferous Huanglong and Chuanshan formations and the Lower Permian Nanlinghu Formation (Peng et al., 2012).

The prolonged tectonic evolution in the Tongling district has formed various structures, including NE-, EW-, NNE-, NS- and NW-trending ones. The NE-trending structures consist of folds and the associated interlayered faults. The EW- and NS-trending structures are mainly basement faults. The NNE-trending structures include small-sized compression shear fracture zones and folds. The NW-trending structures consist of thrust faults and compression fracture zones (Liu et al., 1996). The EW-, NE-, NNE-trending structures are closely associated with the rock- and ore-forming processes.

Granitoid emplacement at Tongling are mainly fault-controlled, and extend along the NE, NNE, NW, EW and NS directions (Fig. 2). These intrusions were dated to be 132–152 Ma (Xu et al., 2008b, 2012), and geochemically belong to: 1) shoshonite series ($SiO_2 \leq 55\%$), comprising monzonite and quartz monzonite, which are closely Au-Ag-Pb-Zn mineralization-related (Wu et al., 2010; 2013); and 2) high-K calc-alkaline series ($SiO_2 > 55\%$), comprising quartz diorite, quartz monzodiorite, granodiorite, quartz monzonite and pyroxene diorite, which are closely Cu-Au-Fe mineralization-related (Wu et al., 2001; Wang et al., 2003; Li et al., 2007; Yang et al., 2008; Wu et al., 2010; Wu et al., 2013). Primary magma of the shoshonitic granitoids was likely alkaline basaltic, which originated from the enriched mantle and then underwent fractional crystallization and minor crustal assimilation (Wang et al., 2003; Li et al., 2007). The high-K calc-alkaline magma was likely a mixture between the mantle-derived magma and crust-derived magma (Du et al., 2010; Wu et al., 2010). Xu et al. (2012) considered that the intrusions at Tongling should belong to the high-K calc-alkaline series.

3. Deposit geology

The Dongguashan Cu-(Au) deposit is situated at the intersection of the EW-trending Tongling-Shatanjiao tectonic-magmatic belt and the Qingshan anticline of the NE-trending Shun'an syncline (Fig. 2) (Xu et al., 2010, Xu et al., 2011). The ore-related sequence consists of quartz sandstone and shale of the Upper Devonian Wutong Formation, (dolomitic) limestone of the Middle-Upper Carboniferous Chuanshan and Huanglong formations, and limestone, quartzite and skarn of the Lower Permian Qixia Formation. Followed by quartzite intercalated with thin clayey limestone of the Upper Permian Dalong Formation, and impure carbonates of the Lower Triassic Helongshan and Nanlinghu

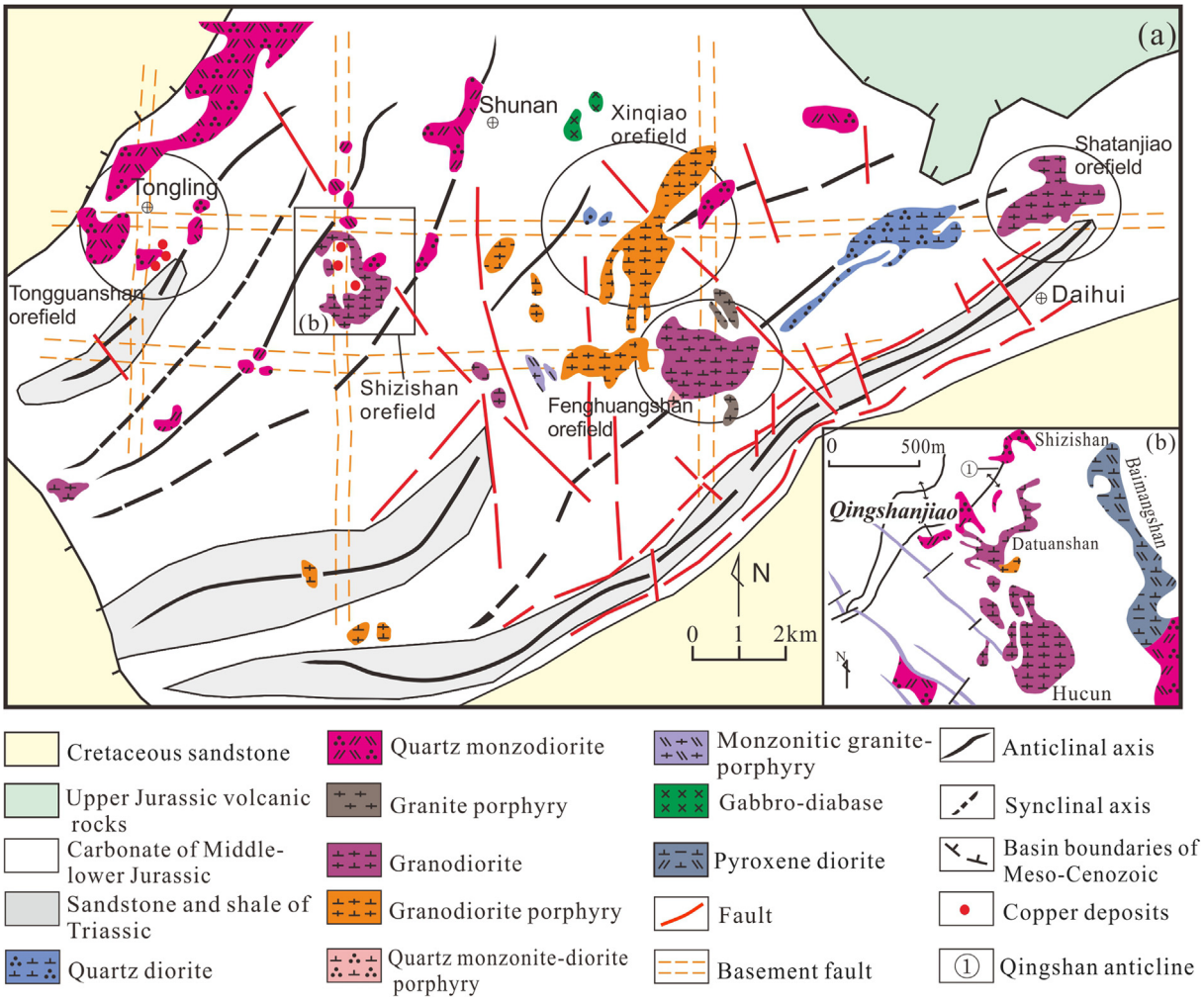

Fig. 2. Geological maps of the (a) Tongling ore district (modified after Peng et al. (2012)) and (b) Shizishan ore field (modified after Xu et al. (2008a)).

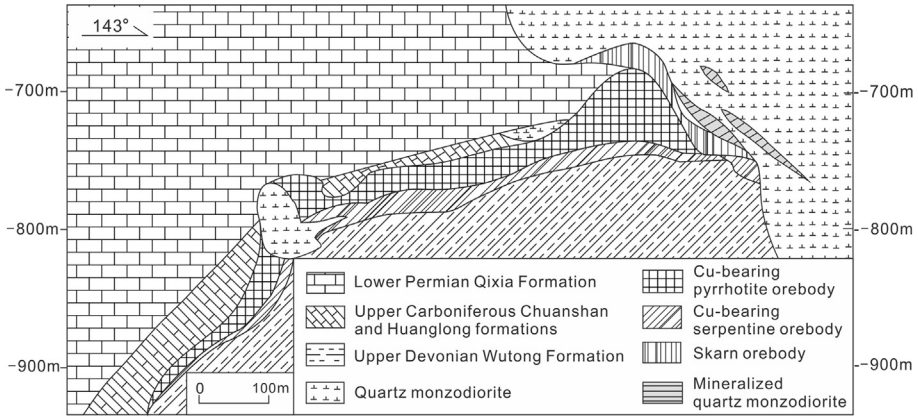

Fig. 3. Geological cross section along Exploration Line No. 50 of the Dongguashan deposit (modified after Guo et al. (2010)).

formations. Major structures include the NE-trending anticlines, the NS-, EW- and NNE-trending faults, and the interlayer fracture zones between the Devonian and Carboniferous formations.

The Qingshanjiao quartz monzodiorite (LA-ICP-MS zircon U-Pb age: 136.7 ± 2.3 Ma; Liu et al., 2018) is the main intrusion at Dongguashan. The rocks are medium- to coarse-grained and porphyritic, and comprise plagioclase (30–35%), K-feldspar (20–30%), quartz (15–20%), and hornblende (10%), with accessory (< 5%) biotite, epidote, and chlorite. Contact metamorphism and hydrothermal alteration are extensively developed around the intrusive body, and the altered minerals including skarn minerals (e.g. andradite, diopside), quartz, K-feldspar, calcite, epidote and chlorite. The ore minerals (e.g., magnetite, pyrrhotite, pyrite, chalcopyrite) are closely related to skarn minerals, quartz and K-feldspar.

The Dongguashan Cu-(Au) deposit contains four types of orebodies: stratiform, porphyry, skarn, and vein-like (Figs. 3 and 4), among them the stratiform orebodies are the most important. Major stratiform orebodies are distributed along the core and limbs of the NE-trending Qingshan anticline, and hosted in the limestone of the Middle and Upper Carboniferous Huanglong and Chuanshan formations. The orebody occurrence is controlled by sedimentary sequence, interlayer fracture, and intrusive contact with the Qingshanjiao pluton (Fig. 3). The thickness and grade of the orebodies increase towards the Qingshanjiao pluton. The ore minerals in these major orebodies are magnetite, pyrrhotite, pyrite and chalcopyrite, with minor bornite, chalcocite, sphalerite, tetrahedrite, molybdenite, galena, and native gold. The gangue minerals include quartz, calcite, garnet and diopside, with minor actinolite, tremolite and anhydrite. Porphyry-type orebodies are mainly located at the top of the Qingshanjiao pluton, with the main ore minerals of pyrite, chalcopyrite and pyrrhotite, gangue minerals of quartz, chlorite, sericite. Skarn-type orebodies are mainly distributed within the intrusive contact between the Qingshanjiao pluton and the carbonate rocks, with the main ore minerals of chalcopyrite, magnetite, pyrrhotite and pyrite, gangue minerals of andradite, chondrodite, tremolite, diopside, epidote and quartz. Vein-like orebodies are situated in the hanging wall and footwall of the major stratiform orebodies, with

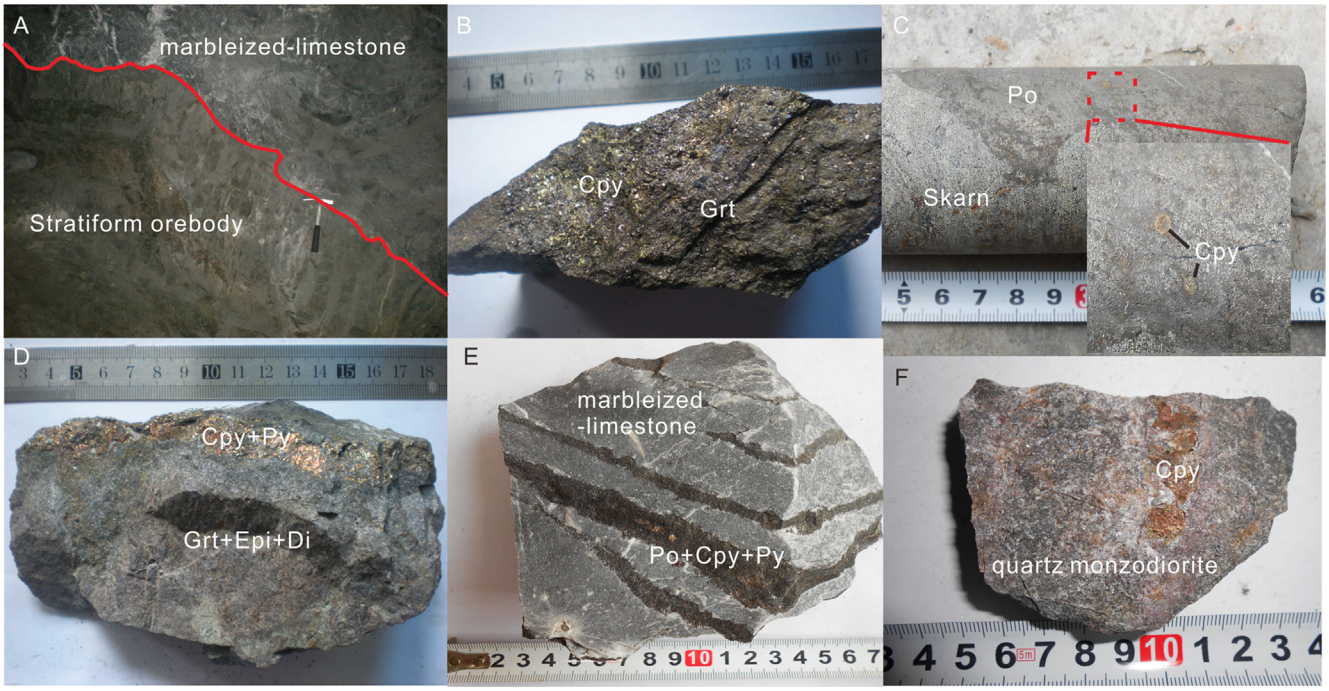

Fig. 4. (A) Stratiform orebody consisting of magnetite, chalcopyrite, pyrite and pyrrhotite. (B) Chalcopyrite in skarn, showing impregnation texture. (C) Massive chalcopyrite ore and chalcopyrite in skarn, showing inclusion texture. (D) Chalcopyrite and pyrite vein in garnet, diopside and epidote, showing filling structure. (E) Chalcopyrite, pyrite and pyrrhotite vein in marbleized limestone. (F) Granular chalcopyrite in quartz monzodiorite. Mt-Magnetite; Cpy-Chalcopyrite; Py-Pyrite; Po-Pyrrhotite; Grt-Garnet; Di-Diopside; Epi-Epidote.

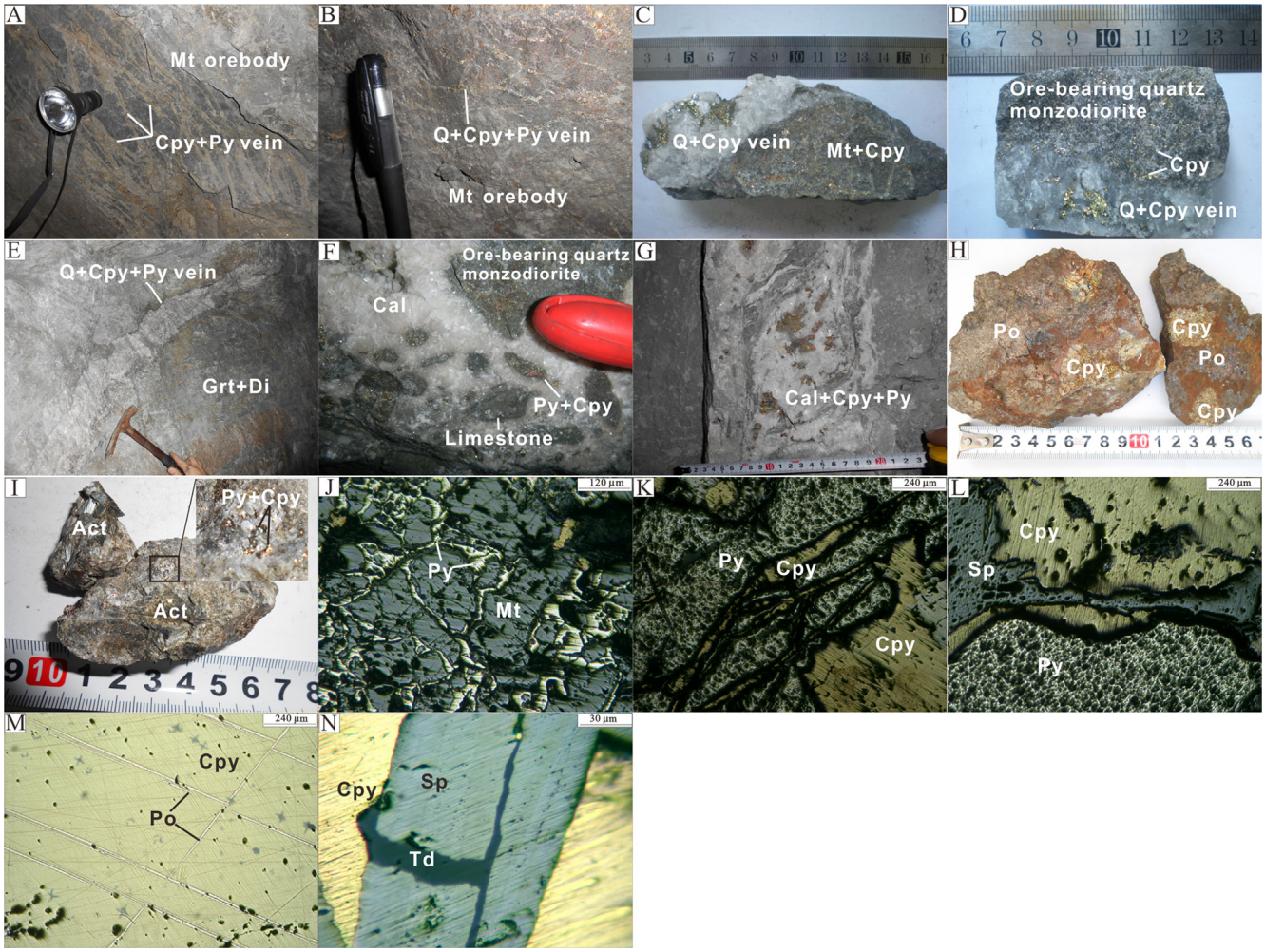

Fig. 5. Photographs and photomicrographs of the Dongguashan Cu-(Au) deposit. A and B. Chalcopyrite-pyrite vein crosscut magnetite orebody. C. Quartz-chalcopyrite vein in chalcopyrite magnetite orebody. D. Quartz-chalcopyrite vein in ore-bearing quartz monzodiorite. E. Quartz-chalcopyrite-pyrite vein in diopside garnet skarn. F. Brecciated limestone, sulfide, and ore-bearing quartz monzodiorite. G. Late calcite-chalcopyrite-pyrite vein. H. Massive chalcopyrite surrounding by pyrrhotite. I. Chalcopyrite- and pyrite-bearing actinolite skarn. J. Pyrite metasomatized magnetite (reflected light, plane polar). K. Vein-like chalcopyrite cutting pyrite (reflected light, plane polar). L. Vein-like sphalerite metasomatized chalcopyrite (reflected light, plane polar). M. Chalcopyrite and pyrrhotite with exsolution texture (reflected light, plane polar). N. Tetrahedrite in-fills in sphalerite. Mt-Magnetite; Cpy-Chalcopyrite; Py-Pyrite; Po-Pyrrhotite; Sp-Sphalerite; Td-Tetrahedrite; Grt-Garnet; Di-Diopside; Epi-Epidote; Act-Actinolite; Cal-Calcite.

the main ore minerals of pyrite, chalcopyrite and pyrrhotite, gangue minerals of quartz. These four types of orebodies have massive, laminated, vein-like, banded, disseminated and brecciated structures and granular, metasomatic and exsolution textures.

Based on field and microscope observations on ore textures and ore/alteration mineral contents and paragenesis (Fig. 5), the mineralization is divided into three stages: (I) prograde skarn, (II) retrograde alteration (main Cu-(Au) mineralization stage) and (III) quartz-carbonate stages. Stage I is composed of andradite, diopside and humite. Stage II is the main mineralization stage, contains predominantly chalcopyrite, pyrite, magnetite, pyrrhotite sphalerite, chalcocite, serpentine, epidote, quartz and talc. Mineralization largely ceased in Stage III, which contains large amount of calcite, quartz and rare ore minerals of chalcopyrite and pyrite.

4. Sampling and analytical methods

4.1. Sample collection

Stage II quartz and Stage III calcite samples for the hydrogen-oxygen (H-O) isotope analyses were collected from the west ore drift along Exploration Line 66 (underground adits of −850 m below sea level (bsl)) and the entrance of the west ore drift along Exploration Line 44 (underground adits of −730 m bsl). Samples for the sulfur-lead isotope analyses were collected from the ore drift along Exploration Lines 59, 64, and 66 (underground adits of −850 m bsl), and Exploration Line 48 (underground adits of −730 m bsl) and drilling core. These samples were collected from different types (stratiform, porphyry-type, skarn-type and vein-like) of orebodies, Qingshanjiao pluton and limestone. Samples for fluid inclusion (FI) analysis were collected from the underground adits (Exploration Lines 59, 64 and 66 at –850 m bsl, and Stope No. 2 at −730 m bsl) at Dongguashan. The fluid inclusion samples include Stage I garnet, Stage II quartz and Stage III calcite.

4.2. Hydrogen-oxygen isotope analyses

The H-O isotope analyses were performed at the Analysis and Testing Research Center of Nuclear Industry (Beijing Institute of Geology) using a Finnigan-MAT253 mass spectrometer. The quartz and calcite samples from the quartz veins and calcite veins were handpicked to ensure > 99% purity. Oxygen was liberated from quartz by reaction with BrF_5 (Clayton and Mayeda, 1963) and converted to CO_2 on a platinum-coated carbon rod for the oxygen isotope analysis. The water of the fluid inclusions in the quartz samples was released by heating the

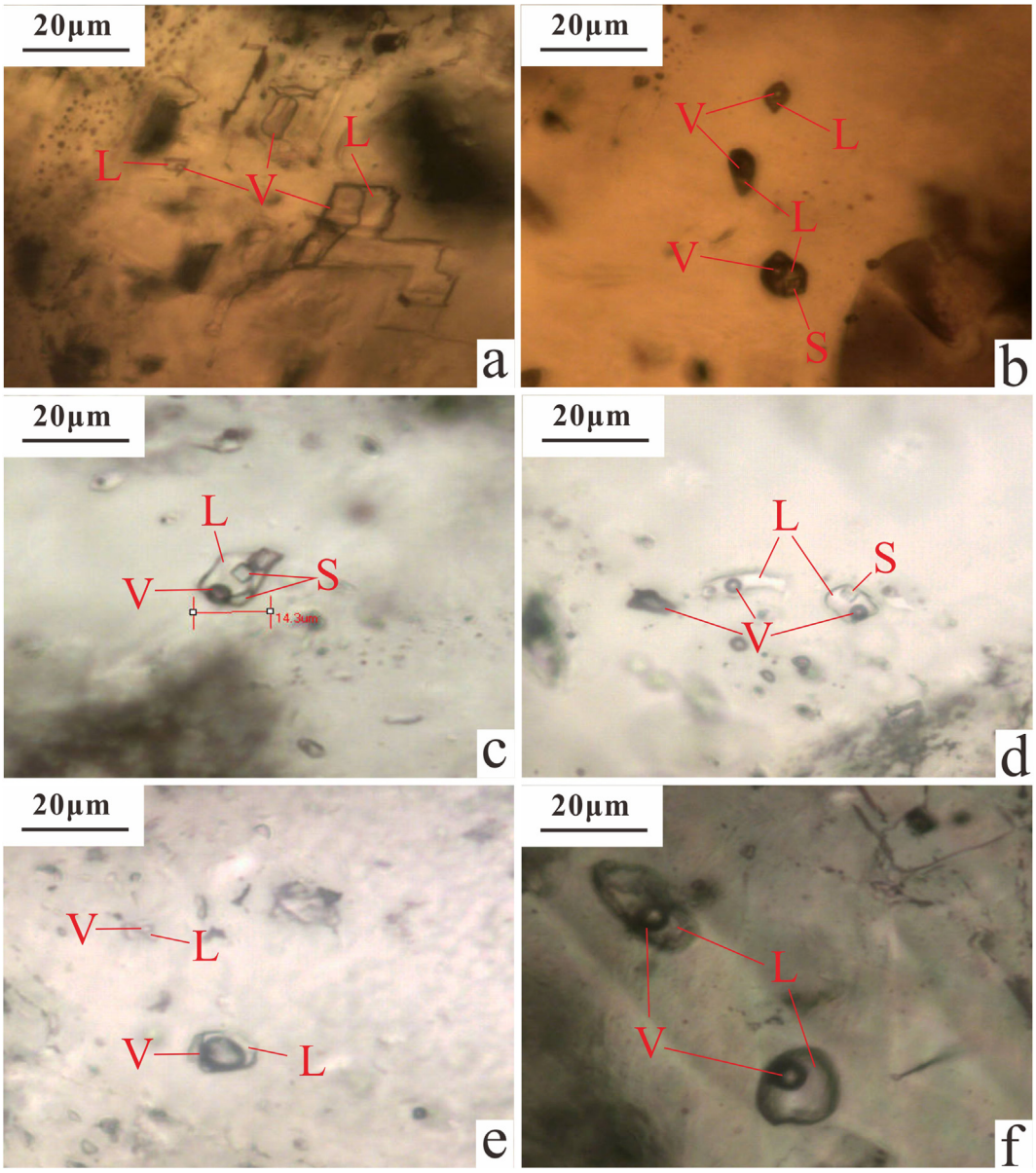

Fig. 6. Microphotographs of fluid inclusions in garnet, quartz and calcite from the Dongguashan Cu-(Au) deposit. (a) Liquid-rich and vapor-rich two-phase aqueous inclusions in garnet. (b) Liquid-rich, vapor-rich aqueous inclusions with daughter minerals in garnet. (c) Aqueous inclusions with multiple daughter minerals (e.g., halite) in quartz. (d) Liquid-rich, vapor-rich aqueous inclusions coexistent with daughter mineral in quartz. (e) Vapor-rich two-phase fluid inclusions in quartz. (f) Liquid-rich two-phase aqueous inclusions in calcite. L-Liquid phase, V-Vapor phase, S-Daughter mineral.

samples to above 500 °C in an induction furnace, and then reacted the fluid inclusions with zinc powder at 410 °C to generate H_2 for the H isotope analysis (Friedman, 1953). Oxygen isotope analysis of calcite was analyzed using the 100% phosphoric acid method (MaCrea, 1950). The calcite was reacted with phosphoric acid to release the CO_2 at 25 °C, and the oxygen isotopic composition was then measured on a Finnigan-MAT 253 mass spectrometer. The H isotope analysis method for calcite was the same as that for quartz. The results are reported in per mil units relative to V-SMOW standard at a precision of ± 2‰ for δD and ± 0.2‰ for $\delta^{18}O$. The $\delta^{18}O_{water}$ values of the ore-forming fluids from the quartz samples were calculated using the equation 1000 $\ln\alpha_{quartz\text{-}water} = 3.38 \times 10^6/T^2 - 3.40$ (Clayton et al., 1972), where α is the fractionation factor and T is the average homogenization temperature of the FIs from Stage II quartz. The $\delta^{18}O_{water}$ values of the ore-forming fluids from the calcite samples were calculated using the equation 1000 $\ln\alpha_{calcite\text{-}water} = 2.78 \times 10^6/T^2 - 3.39$ (O'Neil et al., 1969), where α is the fractionation factor and T is the average homogenization temperature of the FIs from Stage III quartz.

4.3. Sulfur-lead isotope analyses

The S-Pb isotope analyses were performed at the Analysis and Testing Research Center of Nuclear Industry (Beijing Institute of Geology). The pyrite and pyrrhotite samples from the stratiform, porphyry-type, skarn-type and vein-like orebodies were handpicked to achieve > 99% purity. The S isotope analyses were performed using a MAT 253 gas isotope mass spectrometer. The analysis involved the preparation of SO_2 by combustion at 1000 °C with V_2O_5. Corresponding analyses of the sulfate minerals required the preparation of H_2S by reaction with the Kiba solution at 350 °C, which was subsequently converted to Ag_2S and oxidized with V_2O_5 to SO_2 at 1000 °C. The SO_2 was then analyzed by mass spectrometry. Whole-rock S isotopes were analyzed using the sodium carbonate-zinc oxide semi-melting method. The samples were heated to 980 °C under a vacuum of 2.0×10^{-2} Pa,

Table 1
Microthermometric data of fluid inclusions from the Dongguashan copper (gold) deposit.

Stage	Host minerals	FI type	Tm_{ice} (°C) (number)	Tm_S (°C)	Th (°C)	Salinity (wt % NaCl equiv)	Dengsity (g/cm^3)
Prograde skarn alteration (Stage I)	Garnet	I	−7.3 to −13.5 (4)		379.1–482.3 (4)	10.9–17.3	0.49–0.68
		II	−6.0 to −16.0 (9)		389.9–495 (9)	9.2–19.4	0.49–0.68
		III		283–350 (3)	459–512.1 (3)	36.7–42.4	0.88–0.99
	Garnet	I	−6.7 to −16.2 (4)		450–547.5(4)	10.1–19.6	0.33–0.70
		II	−3.6 to −9.6 (10)		318.8–522.1 (10)	5.9–13.5	0.37–0.73
		III		360.1 (1)	500(1)	43.3	0.97
	Garnet	I	−7.7 to −13.2 (2)		401.2–500 (2)	11.3–17.1	0.56–0.58
		II	−5.5 to −13.5 (10)		390.1–500(10)	8.6–17.3	0.47–0.69
		III		338.9–345.5 (2)	450–469.2 (2)	41.5–41.9	0.97–0.99
Retrograde alteration (Stage II)	Quartz	I	−3.2 to −8.4 (6)		286.2–372.5 (6)	5.3–12.2	0.69–0.79
		II	−5.5 to −12.1 (8)		235.2–360.1 (8)	8.6–16.1	0.73–0.86
		IV		245.6 (1)	324	34.4	1.12
	Quartz	I	−0.8 to −10.1 (11)		307–378.2 (11)	1.4–14.0	0.58–0.76
		II	−2.6 to −7.2 (5)		301.9–372.2 (5)	4.3–10.7	0.69–0.76
		III		332.1 (1)	348.6 (1)	40.6	1.06
	Quartz	I	−3.4 to −13.1 (5)		307.0–358.1 (5)	5. 6–17.0	0.64–0.80
		II	−3.8 to −9.8 (9)		258.4–327.6 (9)	6.2–13.7	0.66–0.88
		III		173.5–338.9 (3)	265.1–469.2 (3)	30.7–41.5	1.03–1.07
		IV		335.1 (1)	350.1 (1)	41.0	1.07
Quartz-carbonate alteration (Stage III)	Calcite	II	−5.2 to −12.6 (16)		196.7–263. 2 (16)	8.1–16.5	0.85–1.06

Tm_{ice} = Final melting temperature of ice; Tm_S = Final dissolution temperatures of the halite daughter crystal; Th = Homogenization temperature; Type I: Vapor-rich aqueous inclusions; Type II: Liquid-rich aqueous inclusions; Type III: Daughter-minerals-bearing aqueous inclusions, homogenized to liquid by the disappearance of vapor phase; Type IV: Daughter-minerals-bearing aqueous inclusions, homogenized to liquid by the disappearance of daughter minerals.

SO_2 was generated and frozen collected, and then the S isotope composition was measured with a MAT 253 gas isotope mass spectrometer. The S isotope ratios were reported relative to the CDT (Canon Diablo troilite) standard in the $\delta^{34}S$ notation. The sulfide references were the GBW-04414 and GBW-04415 silver sulfide standards, with $\delta^{34}S$ values of 0.07 ± 0.13‰ and 22.15 ± 0.14‰, respectively. The analytical precision was better than ± 0.2‰ (Li et al., 2014). The Pb isotope analyses were conducted using an IsoProbe-T thermal ionization mass spectrometer (TIMS). The Pb was separated and purified using a conventional cation-exchange technique (AG1 × 8, 200–400 resin) with diluted HBr used as the eluant. The $^{208}Pb/^{206}Pb$, $^{207}Pb/^{206}Pb$, and $^{204}Pb/^{206}Pb$ ratios of the NBS981 Pb standard were 2.1681 ± 0.0008 (2σ), 0.91464 ± 0.00033 (2σ), and 0.059042 ± 0.000037 (2σ), respectively.

4.4. Fluid inclusions

Petrographic observations and temperature measurements of fluid inclusions were undertaken using a Linkam THMSG 600 heating–-freezing stage at the Key Laboratory of Metallogenic Prediction of Nonferrous Metals and Geological Environment Monitoring (Central South University). Analytical precisions were better than ± 1 °C and ± 0.1 °C for temperatures of 30–600 °C and −196 to 30 °C, respectively. Freezing and heating temperatures were measured using the same inclusions where possible, and phase transitions were carefully monitored. During the temperature measurement, temperatures were changed by 5 °C/min and then changed slowly at steps of 0.2 °C/min when approaching the phase transition.

Bulk FI analysis was performed for the gas-liquid-phase compositions, with the single mineral purity being > 89%. The analysis was conducted at the Key Laboratory of Metallogenic Prediction of Nonferrous Metals (Central South University), using a Varian-3400 gas-phase gas chromatograph (Varian) and a DX-120 Ion Chromatography ion chromatograph (Dionen). Analytical error was less than 5%.

5. Results

5.1. Fluid inclusions

5.1.1. Fluid inclusion petrography

The FIs analyzed are mostly primary and 5–40 μm in size. Secondary FIs are not well developed at Dongguashan. In terms of the phase behavior at room temperature, the primary FIs can be divided into four types: vapor-rich two-phase aqueous (Type I), liquid-rich two-phase aqueous (Type II), daughter-minerals-bearing three-phase (Type III, which homogenized to liquid by disappearance of vapor phase), and daughter-minerals-bearing three-phase (Type IV, which homogenized to liquid by disappearance of daughter minerals) (Fig. 6).

Types I and II FIs are commonly found in all Stage I to III. They have irregular and ellipsoidal shapes, with sizes ranging from 5 to 40 μm. Type I FIs represent ~20% of the primary FIs and homogenized to a gaseous phase. Type II FIs are the main FI type, and account for 60% of all primary FIs. They contain 5–30% vapor phase, and homogenized to a liquid phase.

Types III and IV FIs are mainly occurred in Stage I garnet and Stage II quartz. These irregularly-shaped FIs contain 10 to 30% vapor and are 10 to 20 μm in size. Daughter crystals are mainly halite, with a maximum size of 5 μm (Fig. 6).

5.1.2. Fluid inclusion microthermometry and salinity

The salinities of Types I and II FIs were calculated from freezing point temperatures using the following formula (Hall et al., 1988):

$$S = 0.00 + 1.78T - 0.042T^2 + 0.000557T^3$$

where S is the salinity (NaCl in wt%) and T represents the freezing point temperature (°C). The salinities of Type III and IV FIs were obtained from the melting temperature of the daughter minerals (Lu et al., 2004).

The homogenization temperatures and salinities of each FI type are listed in Table 1 and illustrated in a histogram (Fig. 7).

In Stage I garnet, Type I FIs have a wide range of homogenization temperatures 379–548 °C (average 456 °C), with salinities of 10.1–19.6 wt% NaCl equivalent. Type II FIs have homogenized at 319–522 °C (average 453 °C) and with salinities of 5.9–19.4 wt% NaCl equivalent. Type III FIs homogenized at 450–512 °C (average 483 °C) and with salinities of 36.7–43.3 wt% NaCl equivalent.

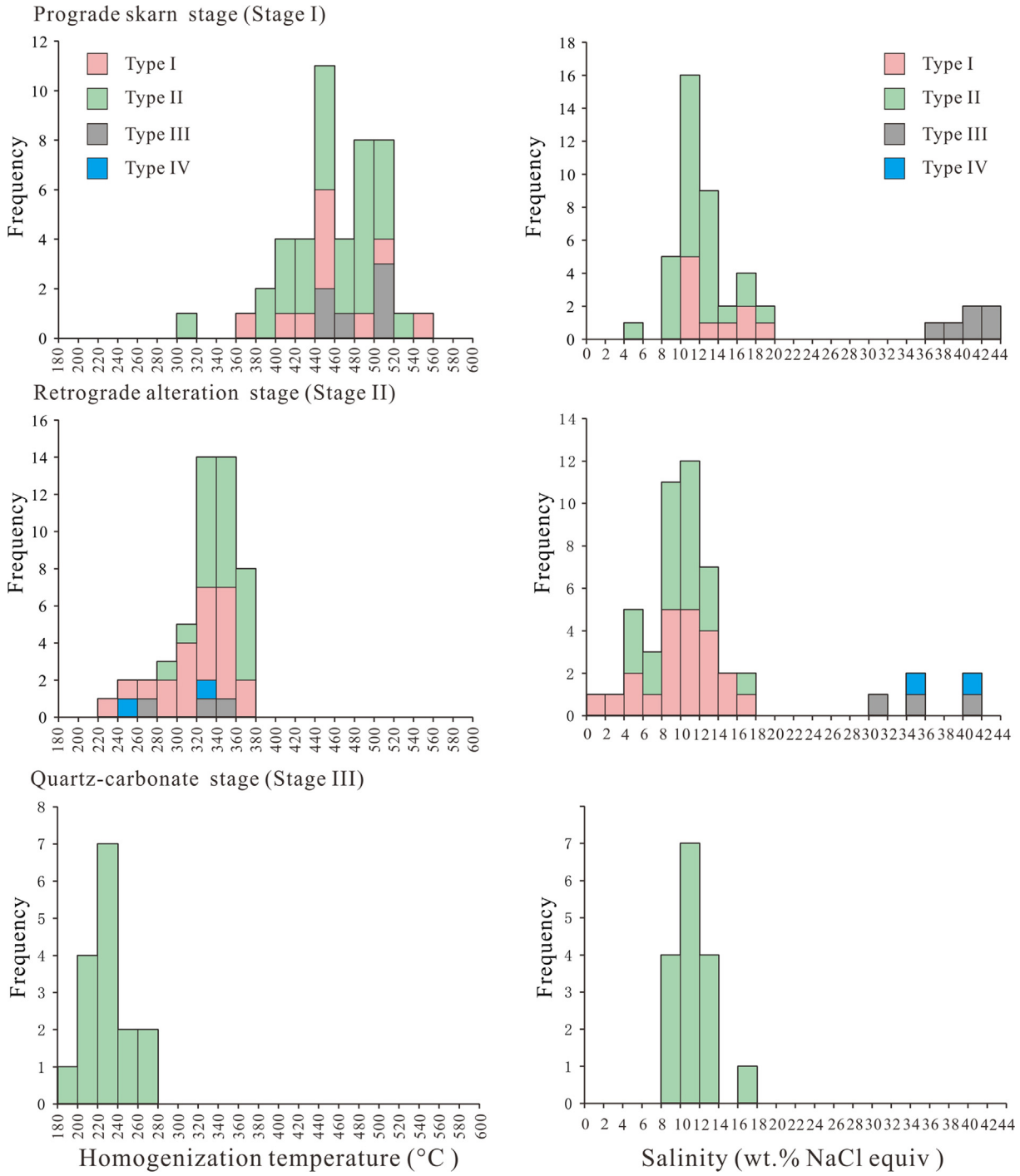

Fig. 7. Homogenization temperatures of primary inclusions, and salinity histograms for all inclusions types, separated into different stages.

In Stage II quartz, Type I FIs homogenized at 286–378 °C (average 346 °C) and with salinities of 1.4–17.0 wt% NaCl equivalent. Type II FIs homogenized at 235–372 °C (average 323 °C) and with salinities of 4.3–16.1 wt% NaCl equivalent. Type III FIs homogenized at 265–349 °C (average 353 °C) and with salinities of 30.7–40.6 wt% NaCl equivalent. Type IV FIs homogenized at 324–350 °C (average 337 °C) and with salinities of 34.4–41.0 wt% NaCl equivalent.

In Stage III calcite, only type II FIs were found, with homogenization temperatures of 197–263 °C (average 229 °C) and salinities of 8.1–16.5 wt% NaCl equivalent.

5.1.3. Fluid inclusion density and pressure estimation

In Stage I and II, the Types I to IV FIs were contemporaneously trapped and formed primary FI clusters. These FIs exhibit similar homogenization temperatures but diverse homogeneity. Therefore, the estimated pressure can represent the actual trapping pressure for the FIs. The Stage I and II trapping pressures, estimated with the FLINCOR program (Brown, 1989), are 219–661 bar and 26–190 bar, respectively. We obtained similar pressure ranges for the prograde skarn and retrograde-altered stages on the Fig. 8, which shows that it is feasible to use the FLINCOR program to calculate the trapping pressure of fluid inclusion. Trapping pressure of Stage III was estimated to be 17–48 bar. The density equation $\rho = A + BT_h + CT_h^2$ $(A = A_0 + A_1w + A_2w^2,$

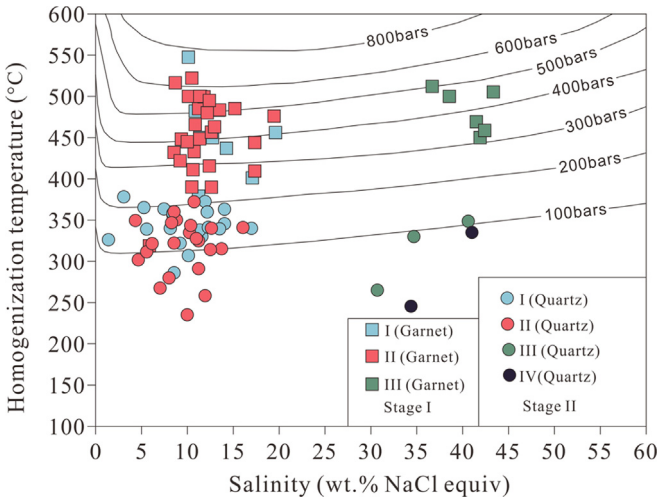

Fig. 8. Pressure estimations for primary Stage I and II fluid inclusions. Type I to IV inclusions of Stage I and II were trapped under immiscible conditions, thus the estimated pressures can represent the actual trapping pressure for the fluids under immiscible conditions.

$B = B_0 + B_1w + B_2w^2$, $C = C_0 + C_1w + C_2w^2$ (where $A_{0\text{-}2}$, $B_{0\text{-}2}$, and $C_{0\text{-}2}$, are dimensionless parameters; T_h and w are the homogenization temperature and salinity, respectively) by Liu and Duan (1987) and Liu (2001) was used to calculate the densities of Types I to IV FIs. In Stage I, the densities of Types I, II and III FIs are 0.33–0.70, 0.37–0.73 and 0.89–0.99 g/cm^3, respectively. In Stage II, the densities of Types I, II, III and IV FIs are 0.58–0.80, 0.66–0.88, 1.03–1.07 and 1.07–1.12 g/cm^3, respectively. In Stage III, the densities of Type II FIs range from 0.85 to 1.06 g/cm^3.

5.1.4. Vapor and liquid compositions of fluid inclusions

The FI vapor and liquid compositions are listed in Table 2. The vapor compositions were mainly gaseous H_2O and CO_2, with some H_2 and CH_4. Comparing the vapor compositions of FIs in Stage I garnet, Stage II quartz and Stage III calcite, it is found that the Stage II FIs contain C_2H_2 and C_2H_4, which are absent in both Stage I and III FIs. Contents of other gases (H_2O, H_2) are also the highest in Stage II FIs.

In the liquid phase, the compositions include mainly Ca^{2+}, Na^+, K^+, SO_4^{2-}, Cl^- and F^-. Among the cations, the Ca^{2+} content is the highest (followed by Na^+) and the K^+ content is the lowest. Among the anions, the SO_4^{2-} content is the highest (followed by Cl^-), and the F^- content is the lowest.

5.2. Hydrogen-oxygen isotopes

The H-O isotope results are listed in Table 3. The measured quartz δD values range from −84.0 to −71.5‰, and $\delta^{18}O$ values from +10.2 to +14.9‰. The measured calcite δD values range from −70.7 to −60.9‰, and $\delta^{18}O$ values from +12.1 to +12.3‰. Oxygen isotope compositions of the hydrothermal fluids ($\delta^{18}O_{H2O}$) from quartz were calculated using the equation of $\delta^{18}O_Q$-$\delta^{18}O_{H2O} = 3.38 \times 10^6/T^2 - 3.40$ (Clayton et al., 1972), together with the measured $\delta^{18}O$ values and the corresponding FI homogenization temperatures for each quartz sample (Table 1). The calculated $\delta^{18}O_{H2O}$ values are +4.51 to +8.97‰. Oxygen isotope compositions of the hydrothermal fluids ($\delta^{18}O_{H2O}$) from calcite were calculated using the equation of $\delta^{18}O_{calcite}$-$\delta^{18}O_{H2O} = 3.38 \times 10^6/T^2 - 3.40$ (O'Neil et al., 1969), together with the measured $\delta^{18}O$ values and the corresponding FI homogenization temperatures for each calcite sample (Table 1). The calculated $\delta^{18}O_{H2O}$ values are +4.41 to +4.91‰.

5.3. Sulfur-lead isotopes

Sulfur isotopes of the various types of orebodies, granitoids and wall rocks (Table 4) were compared to ascertain the source of ore-forming materials at Dongguashan. Our results show that the $\delta^{34}S$ values of pyrite and pyrrhotite from the stratiform orebodies range from +4.1 to +5.3‰ (average +4.8‰), whilst that of one pyrite sample from the skarn orebody is +4.9‰. The pyrite $\delta^{34}S$ values of the vein-like orebodies range from +4.2 to +5.5‰ (average +5.1‰), whilst those of the porphyry orebodies range from +5.1 to +5.7‰ (average +5.4‰). $\delta^{34}S$ values of the quartz monzodiorite and limestone range from −2.20 to +5.02‰ (average +1.40‰) and −4.6 to –29.5‰ (average −17.2‰), respectively.

The S isotope distribution diagram (Fig. 9) demonstrates that the S isotope compositions of the different ore types at Dongguashan are similar to those of the Qingshanjiao pluton, but are markedly different from those of the wall rocks.

Lead isotope compositions of the different types of orebodies are shown in Table 5. The pyrite $^{208}Pb/^{204}Pb$, $^{207}Pb/^{204}Pb$, and $^{206}Pb/^{204}Pb$ ratios of the veil-like orebodies are 38.037 to 38.358, 15.549 to 15.664, and 18.132 to 20.507, respectively. The Pb isotope ratios of one pyrite from the skarn orebody are 38.356, 15.608, and 18.504, respectively. The $^{208}Pb/^{204}Pb$, $^{207}Pb/^{204}Pb$, and $^{206}Pb/^{204}Pb$ ratios for the pyrite and pyrrhotite of stratiform orebodies are 38.052 to 38.448, 15.513 to 15.614, and 18.162 to 18.518, respectively. The pyrite in the porphyry orebodies have $^{208}Pb/^{204}Pb$, $^{207}Pb/^{204}Pb$, and $^{206}Pb/^{204}Pb$ ratios of 38.114 to 38.356, 15.531 to 15.612, and 18.085 to 18.537, respectively. The Pb isotope compositions of the Dongguashan Cu-(Au) ores are similar to those of the feldspar of the granitoids in the Tongling district ($^{208}Pb/^{204}Pb$ = 38.090–38.460, $^{207}Pb/^{204}Pb$ = 15.470–15.600, $^{206}Pb/^{204}Pb$ = 17.940–18.420) (Tang et al., 1998), which indicates that the Dongguashan Cu-(Au) ores may have shared similar Pb source with the intermediate-felsic intrusions in Tongling.

Table 2
Vapor and liquid phase composition (ppm) of fluid inclusions from the Dongguashan copper (gold) deposit.

Mineral	Gaseous phase						Liquid phase						CO_2/H_2O
	H_2	CH_4	CO_2	C_2H_2	C_2H_6	H_2O	F^-	Cl^-	SO_4^{2-}	Na^+	K^+	Ca^{2+}	
Garnet	1.584	16.977	107.253	–	–	1630	0.035	3.253	8.624	1.2	0.525	7.156	0.07
Garnet	2.714	2.625	313.197	–	–	1968	0.019	2.719	7.261	0.972	0.264	9.292	0.16
Garnet	3.389	9.66	51.116	–	–	1230	0.027	3.062	9.162	1.418	0.817	6.267	0.04
Quartz	3.586	17.672	335.876	0.868	–	1867	0.048	2.585	7.172	0.825	0.358	8.693	0.18
Quartz	2.809	15.928	508.189	0.976	0.081	1967	0.039	2.769	7.456	0.764	0.193	7.055	0.26
Quartz	5.023	16.812	586.262	0.411	2.745	1708	0.021	3.256	6.175	0.963	0.217	8.926	0.34
Calcite	1.183	9.081	175.279	–	–	1176	0.03	3.192	2.108	0.724	0.315	8.297	0.15

– Not measured data.

Table 3
Hydrogen and oxygen isotopic compositions of the Dongguashan copper deposit.

Mineralization stage	Sample no.	Mineral	$\delta D_{V\text{-}SMOW}$ (‰)	$\delta^{18}O_{V\text{-}SMOW}$ (‰)	$\delta^{18}O_{H2O}$ (‰)	Th (°C)	Data sources
Retrograde alteration	DK01-2	Quartz	−71.50	10.20	4.51	337	This study
	HS01-10	Quartz	−72.30	11.40	6.06	349	This study
	HS01-11	Quartz	−83.10	13.50	7.80	337	This study
	TS04-2	Quartz	−84.00	14.90	8.97	329	This study
	S10-1	Quartz	−59.30	11.23	6.33	365	Xu et al. (2007)
	S10-2	Quartz	−66.00	12.50	8.40	398	Xu et al. (2007)
	S13	Quartz	−59.90	12.09	7.59	381	Xu et al. (2007)
	S13-2	Quartz	−71.30	11.53	6.23	350	Xu et al. (2007)
	S14	Quartz	−62.70	10.43	5.13	350	Xu et al. (2007)
Quartz-carbonate alteration	MS-7	Quartz	−65.60	11.00	5.29	256	Xu et al. (2007)
	MS-9	Quartz	−60.80	11.30	5.59	250	Xu et al. (2007)
	MS-1	Quartz	−65.10	11.10	3.17	260	Xu et al. (2007)
	MS-2	Quartz	−73.00	14.90	6.97	270	Xu et al. (2007)
	DK02-3	Calcite	−70.70	12.10	4.91	239	This study
	DK02-7	Calcite	−60.90	12.30	4.41	223	This study

Table 4
Analytical results of sulfur isotope compositions from the Dongguashan copper (gold) deposit.

Sample no.	Mineral	Host orebody/rock	$\delta^{34}S_{V\text{-}CDT}$ (‰)	Sample no.	Mineral	Host orebody/rock	$\delta^{34}S_{V\text{-}CDT}$ (‰)
DGS20	Pyrite	vein-like orebody	4.8	DGS006	Pyrrhotite	Stratiform orebody	5.3
DGS20-1	Pyrite	vein-like orebody	4.6	DGS17	Pyrrhotite	Stratiform orebody	4.9
DGS02-8	Pyrite	vein-like orebody	5.6	ZK-24	Pyrite	Porphyry orebody	5.7
DGS21-1	Pyrite	vein-like orebody	5.7	DGS002-4	Pyrite	Porphyry orebody	5.3
ZK-21	Pyrite	vein-like orebody	5.4	DGS002-5	Pyrite	Porphyry orebody	5.1
DGS03-6	Pyrite	vein-like orebody	4.2	ZK1-1	Whole rock	Quartz monzodiorite	−2.2
ZK-15	Pyrite	Skarn orebody	4.9	ZK1-2	Whole rock	Quartz monzodiorite	1.2
DGS17	Pyrite	Stratiform orebody	4.1	ZK1-3	Whole rock	Quartz monzodiorite	5.2
DGS17-3	Pyrite	Stratiform orebody	4.9	DGS1-2	Whole rock	Limestone	−4.6
DGS005-12	Pyrite	Stratiform orebody	5.3	DGS5-1	Whole rock	Limestone	−17.4
DGS004-12	Pyrite	Stratiform orebody	4.5	DGS15	Whole rock	Limestone	−29.5

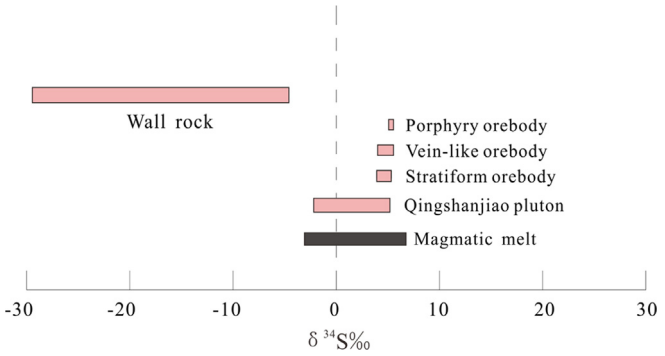

Fig. 9. Sulfur isotope compositions from the Dongguashan Cu-(Au) deposit.

6. Discussion

6.1. Origin of the ore-forming fluids and metals

The obtained δD and $\delta^{18}O_{H2O}$ values of the quartz (−84.0 to −71.5‰ and +4.51 to +8.97‰, respectively) and calcite (−70.7 to −60.9‰ and +4.41 to +4.91‰, respectively) are consistent with those of normal magmatic water (δD = −80 to −40‰, $\delta^{18}O_{H2O}$ = +5.5 to +9.5‰; Sheppard, 1986; Hedenquist et al., 1994). The Dongguashan data points are plotted adjacent to the primary magmatic water field on the δD vs. $\delta^{18}O_{H2O}$ diagram (Fig. 10), which indicates that the ore-forming fluids were mainly magmatic-derived. A salinity of > 30 wt% NaCl equivalent commonly implies that the ore-forming fluids are generally magmatic. In Stage I and II, the maximum salinities of the ore-forming fluids are 43.3 and 41.0 wt% NaCl equivalent, resembling typical magmatic fluids. The CO_2/H_2O ratios of the Dongguashan ores range from 0.04 to 0.34 (Table 2), again resembling common magmatic fluids (< 0.50; Lin, 1986). This supports that the Dongguashan ore-forming fluids were largely magmatic.

Ohmoto (1972) suggested that when the pyrite-pyrrhotite-calcite assemblage is present, the average pyrite $\delta^{34}S$ value approximates the fluid $\delta^{34}S$ value, which is the case at Dongguashan. The Dongguashan pyrite $\delta^{34}S$ values vary in the range of +4.1 to +5.7‰ (average +5.0‰), no matter which ore types the pyrite is from. Both the pyrite $\delta^{34}S$ values and the whole-rock $\delta^{34}S$ values of the intrusion (–2.2 to +5.2‰) fall into the range of typical magmatic fluids (–3.0 to +7.0‰; Ohmoto, 1986; Ohmoto et al., 1997), which demonstrates that the sulfur of the different rock and ore types are largely magmatic. The S isotopes of the Dongguashan rocks and ores also mimic those from the typical skarn deposits in the MLYRB, such as Tongguanshan and Tianmashan, thereby reaffirming a similar magmatic sulfur source in the Tongling ore district (Figs. 11 and 12).

There is little difference in Pb isotopes among the different orebody types, indicating a similar lead source. Fig. 13 shows that most of the Dongguashan data points fall below the orogenic belt growth line, which indicates that the lead is mainly mantle- or lower crustal-derived and implies source mixing (Stacey et al., 1983). The Pb isotope values are similar to those of the feldspar (9.1–9.6; Zhang, 1988) from the Mesozoic granitoids in the MLYRB. This indicates that the different Dongguashan ore types may have shared a common Pb source with the Mesozoic granitoids in the MLYRB (Fig. 14). Fig. 14 illustrates that the data points of the ore samples all fall into the magmatic field (3a), indicating an igneous-related lead source.

6.2. Ore-forming fluid immiscibility

In hydrothermal fluid system, fluid immiscibility can be triggered by: (a) entering of original fluids into open-space structure. The sudden pressure release would trigger fluid immiscibility (boiling); (b) Mixing

Table 5
Analytical results of lead isotope compositions from the Dongguashan copper (gold) deposit.

Sample no.	Mineral	Host orebody	$^{208}Pb/^{204}Pb$	$^{207}Pb/^{204}Pb$	$^{206}Pb/^{204}Pb$	μ	△β	△γ	Th/U
DGS20	Pyrite	vein-like orebody	38.351	15.613	18.528	9.48	18.59	27.66	3.64
DGS20-1	Pyrite	vein-like orebody	38.346	15.610	18.533	9.47	18.37	27.20	3.64
DGS02-8	Pyrite	vein-like orebody	38.358	15.610	18.506	9.47	18.45	28.38	3.66
DGS21-1	Pyrite	vein-like orebody	38.037	15.549	18.132	9.39	15.36	28.33	3.70
ZK-21	Pyrite	vein-like orebody	38.280	15.562	18.312	9.40	15.67	29.84	3.71
DGS03-6	Pyrite	vein-like orebody	38.280	15.664	20.507	9.90	21.54	21.60	2.85
ZK-15	Pyrite	Skarn orebody	38.356	15.608	18.504	9.47	18.31	28.28	3.65
DGS17	Pyrite	Stratiform orebody	38.092	15.516	18.189	9.32	12.81	26.20	3.69
DGS17-3	Pyrite	Stratiform orebody	38.173	15.571	18.477	9.40	15.79	22.20	3.59
DGS005-12	Pyrite	Stratiform orebody	38.354	15.585	18.273	9.45	17.43	34.33	3.77
DGS004-12	Pyrite	Stratiform orebody	38.448	15.580	18.411	9.42	16.62	32.17	3.74
DGS006	Pyrrhotite	Stratiform orebody	38.052	15.513	18.162	9.32	12.69	25.83	3.68
DGS17	Pyrrhotite	Stratiform orebody	38.350	15.614	18.518	9.48	18.69	28.00	3.65
ZK-24	Pyrite	Porphyry orebody	38.356	15.612	18.537	9.47	18.50	27.46	3.64
DGS002-4	Pyrite	Porphyry orebody	38.240	15.545	18.413	9.36	14.15	24.60	3.64
DGS002-5	Pyrite	Porphyry orebody	38.114	15.531	18.085	9.36	14.25	30.95	3.76

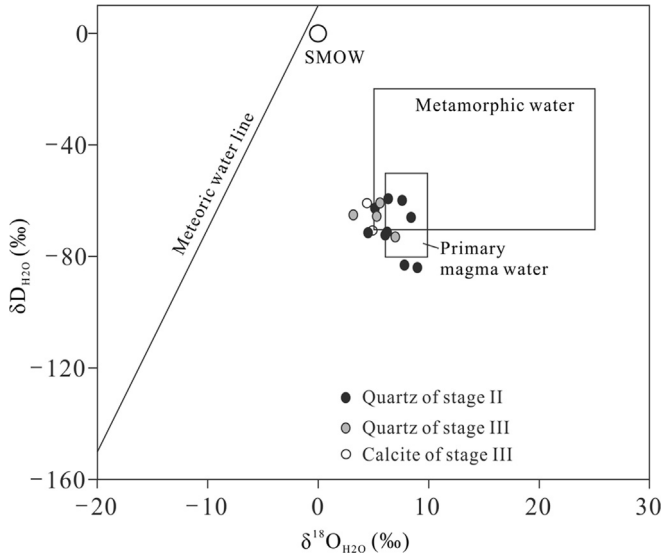

Fig. 10. δD vs. $\delta^{18}O_{H2O}$ for ore-forming fluids from the Dongguashan Cu-(Au) deposit (base diagram from Sheppard (1986)). Meteoric water line from Epstein et al. (1965). Data are as listed in Table 4.

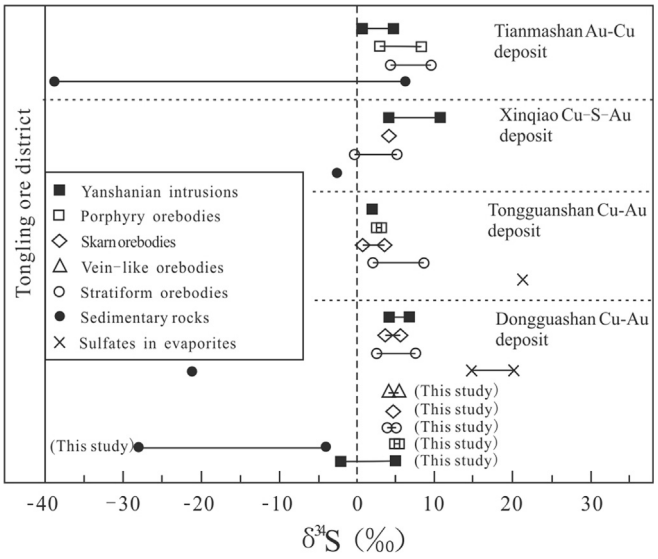

Fig. 11. Comparison of $\delta^{34}S$ values in the Yanshanian (Jurassic-Cretaceous) intrusions, orebodies of various types, Cambrian-Triassic sedimentary rocks and sulfates in evaporites from the major deposits in Tongling district (modified from Pan and Dong (1999)).

of original high-temperature and high-pressure fluids with low-temperature and low-pressure fluids. The sudden temperature drop would lead to fluid immiscibility (boiling); and (c) the involvement of additional components or change in the fluid compositions can also cause fluid immiscibility (Zhang et al., 1996; Lu et al., 2004).

Both Stage I and II are characterized by the co-existence of Type I to III FIs. Along Exploration Line 66 (underground adit of −850 m bsl), angular breccia clasts of the wall rocks and intrusion are observed to be cemented by late calcite (Fig. 15). This is also an important indicator for fluid immiscibility. Therefore, we conclude that fluid immiscibility occurred in Stage I and II.

6.3. Characteristics and evolution of ore-forming fluids

Hydrogen and oxygen isotope compositions of the four FI types suggest that the fluids were likely originated from magmatic water. Type I and II FIs have medium-high temperatures and medium-low salinities. Type III and IV FIs have high temperatures and salinities. From Stage I to III, the temperatures and salinities of Type I and II FIs decrease (Figs. 7 and 8), and the densities increase. Type III FIs dominate the FIs in Stage I garnet, which homogenized to liquid by the disappearance of the vapor bubble. The homogenization temperatures of Type III FIs are 100 °C higher than the melting temperatures of the daughter minerals, indicating that the early-stage magmatic fluids were of high temperature and salinity.

Fluid inclusion micro-thermometric results show that the homogenization temperature, salinity and pressure decrease along with the ore-forming fluid evolution (Figs. 7 and 8). There are clear decreasing trends of temperatures and salinities from the early to late stages (Figs. 8 and 16). Stage III was dominated by gas-rich inclusions, which indicates that the ore-forming fluids had changed from multiphase inhomogeneous fluid to vapor-rich homogeneous fluid.

6.4. Ore-forming mechanism

Fluid immiscibility causes phase separation of a homogeneous fluid into two-/multi-phase heterogeneous fluids, which destroys the original fluid system equilibrium and leads to the mineral precipitation. Fluid boiling is an important ore mineral precipitation mechanism for many types of ore deposits (Roedder, 1984; Drummond and Ohmoto, 1985; Zhang 1997; Cox et al., 2001; Hagemann and Luders, 2003; Chen et al., 2007; Klemm et al., 2008).

Under the high-temperature and high-pressure conditions of the

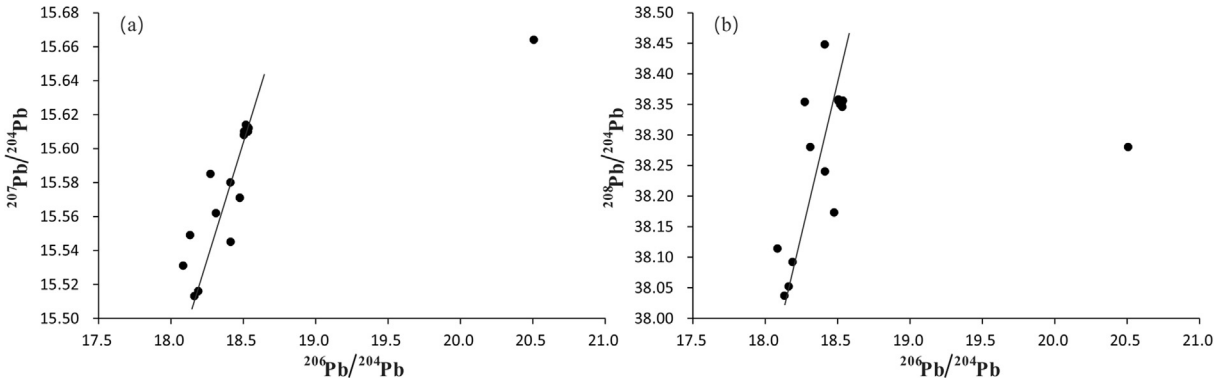

Fig. 12. Diagram of $^{206}Pb/^{204}Pb$ vs. $^{207}Pb/^{204}Pb$ and $^{206}Pb/^{204}Pb$ vs. $^{208}Pb/^{204}Pb$.

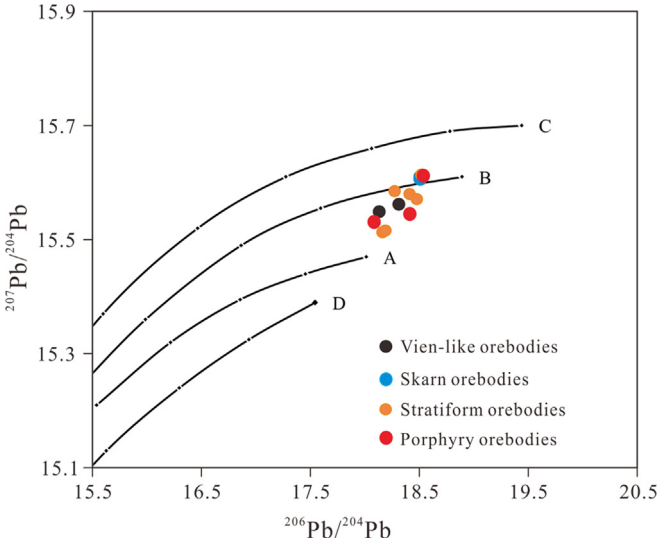

Fig. 13. Plumbotectonic model for the Dongguashan Cu-(Au) deposit (base map after Zartman and Doe (1981)) (A-Mantle; B-Orogen; C-Upper Crust; D-Lower Crust).

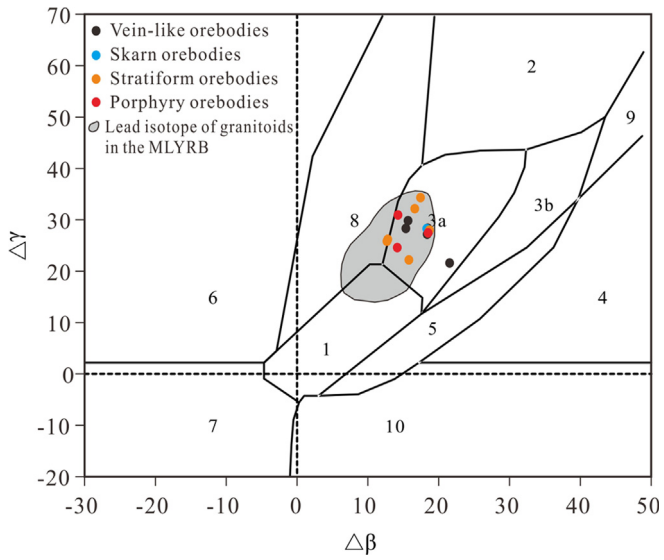

Fig. 14. Δβ vs. Δγ diagram of lead isotopes (after Zhu et al. (1998)). 1-Mantle source lead; 2-Upper crust lead; 3-Subduction-zone lead of mixed upper crust and mantle source (3a-Magmatism; 3b-Sedimentary); 4- Lead from chemical deposition; 5-Lead from submarine hydrothermalism; 6-Lead from medium-deep metamorphism; 7-Deep metamorphism of lower crust lead; 8-Orogen lead; 9-Ancient shale upper crustal lead; 10-Retrograde lead. The granitoids field is drawn using data from Li (2004), Ma and Shan (1996), Xie (2008) and Yan et al. (2003).

early stage (Stage I), CO_2 was totally miscible with the hydrothermal fluids. As the fluids ascended to the shallow part of the crust and entered the interlayer fracture zones, the sudden pressure release and temperature drop may have increased the H^+ and S^- concentrations (by increasing the H_2S solubility). This pushed the reaction of Eq. (1) to the left and produced a large amount of CO_2 and H_2O (Hu and Yang, 2003). Immiscibility occurred and gaseous CO_2 and H_2O were separated from the aqueous fluid (Hu and Yang, 2003), causing sulfide (e.g., chalcopyrite and pyrite) precipitation (Williams-Jones and Ferreira, 1989; Cox et al., 2001; Hagemann and Luders, 2003). The leftward shift of the reaction in Eq. (1) consumed a large amount of H^+, and the remaining S^- may have combined with Cu^{2+} and Fe^{2+} to form sulfides such as chalcopyrite and pyrite.

$$CO_2 + H_2O \rightleftharpoons H_2CO_3 \rightleftharpoons H^+ + [HCO_3]^- \rightleftharpoons 2H^+ + CO_3^{2-} \quad (1)$$

The Middle-Triassic to Cenozoic period was likely an intraplate deformation period in the Tongling area. The basic tectonic framework may have formed during the Indosinian (Triassic) period, dominated by NE-striking S-shaped folds and interlayer fracture zones. Due to the Yanshanian (Jurassic-Cretaceous) tectonic influence, rocks in the area were dominated by block-faulted. This led to widespread extensive granitoid emplacement and the associated hydrothermal alteration. At Stage I, high-temperature homogeneous magmatic-derived fluid may have ascended along the faults into the interlayer fracture zones between the Carboniferous Huanglong and Chuanshan formations. The abrupt pressure release may have caused fluid immiscibility (boiling) and led to the formation of inhomogeneous fluids. This inhomogeneous fluid was ca/ptured by Stage I skarn minerals (e.g., andradite) formed by contact metasomatism. With the ore-forming fluid continued to evolve, Stage I skarn minerals (e.g., andradite) experienced retrograde alteration and released Fe into the fluid, which contributed to magnetite mineralization under high temperatures (Xu et al., 2005). During this process, the rapid temperature and pressure drop, external fluid incursion, and compositional changes in the fluid may have caused a second fluid boiling. This caused the loss of volatiles (such as CO_2 and H_2O) and pH increase, which destabilized the metal complexes and promoted sulfide precipitation in favorable chemical/structural traps (Rui et al., 1984; Li et al., 1999; Xie et al., 2005). The retrograde alteration is strong along fractures and discordant boundary at Dongguashan. The early magnesian skarn was altered into an assemblage of serpentine, talc, pyrite, chalcopyrite and pyrrhotite. At Stage III, external fluid incursion intensified, which cooled down the ore-forming fluid system. Only minor H_2S remained and reacted with Fe^{2+} and Cu^{2+} to form sulfides. In summary, Stage I and II are the main mineralization stages at Dongguashan. Minor Stage III mineralization has likely superimposed on the earlier orebodies and further upgraded the ores.

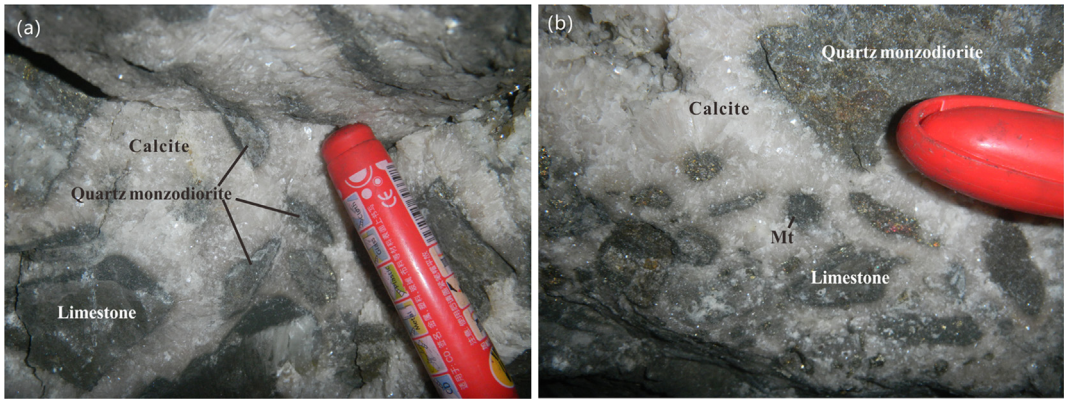

Fig. 15. Photos of (a) calcite cemented quartz monzodiorite and limestone; and (b) calcite cemented quartz monzodiorite, limestone and magnetite. Abbreviation: Mt-Magnetite.

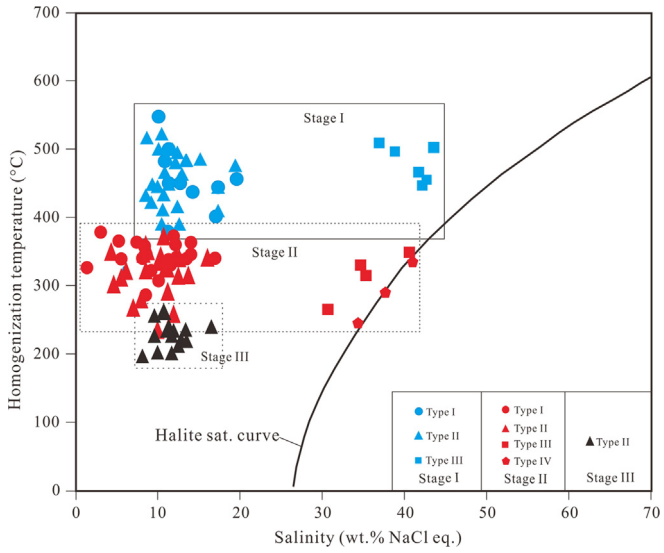

Fig. 16. Homogenization temperature vs. salinity of fluid inclusions in different stages of the Dongguashan Cu-(Au) deposit (after Bodnar (1983)).

7. Conclusions

(1) Ore-forming process in the Dongguashan Cu-(Au) deposit can be divided into three stages: (I) prograde skarn alteration, (II) retrograde alteration, and (III) quartz-carbonate alteration.
(2) Fluid inclusions of the Dongguashan deposit are primarily vapor-rich two-phase (Type I), liquid-rich two-phase (Type II), and daughter-minerals-bearing aqueous inclusions (Type III and IV). Coexistence of Type I to IV FIs in Stage I and II indicate that magmatic fluid immiscibility was likely the predominant mechanism of Cu-(Au) precipitation. From Stage I to III, the ore-forming fluids show a decreasing trend of homogenization temperature and salinity.
(3) Hydrogen-oxygen isotope compositions indicate that the ore-forming fluids of the Dongguashan deposit were principally magmatic-derived. Sulfur and Pb isotopes suggest that the ore-forming materials were derived from a deep-seated magmatic source.
(4) Deposit geology, FIs and H-O-S-Pb isotopic data indicate that Dongguashan is a Cu-(Au) skarn deposit.

Acknowledgments

This study was supported by the National Natural Science Foundation of China (Grant No. 41702078). We are grateful to editors, Huayong Chen and Franco Pirajno, and two anonymous reviewers for their critical and constructive comments and suggestions, which significantly helped to improve this paper.

References

Bodnar, R.J., 1983. A method of calculating fluid inclusion volumes based on vapor bubble diameters and PVTX properties of inclusion fluids. Econ. Geol. 78, 535–542.
Brown, P.E., 1989. FLINCOR: a microcomputer program for the reduction and investigation of fluid-inclusion data. Am. Mineral. 74, 1390–1393.
Cao, Y., Du, Y.S., Pang, Z.S., Ren, C.L., Du, Y.L., Xiao, F.Q., Zhou, G.B., Chen, L.J., 2016. Sulfide zonal texture and its geological significance of ores from the Dongguashan copper (gold) deposit in Tongling. Anhui Province. China. Acta. Petrol. Sin. 32, 334–350 in Chinese with English abstract.
Cao, Y., Gao, F.P., Du, Y.S., Du, Y.L., Pang, Z.S., 2017. Genesis of the Datuanshan stratabound skarn Cu(–Mo) deposit, Middle-Lower Yangtze Valley, Eastern China: constraints from geology, Re–Os geochronology, mineralogy, and sulfur isotopes. Miner. Deposita 3, 443–462.
Chang, Y.F., Liu, X.P., Wu, C.Y., 1991. In: The Copper – Iron Belt of the Lower and Middle Reaches of the Changjiang River. Geological Publishing House, Beijing, pp. 379 in Chinese with English abstract.
Chen, Y.J., Ni, P., Fam, H.R., Pirajno, F., Lai, Y., Su, W.C., Zhang, H., 2007. Diagnostic fluid inclusions of different types hydrothermal gold deposits. Acta. Petrol. Sin. 23, 2085–2108 in Chinese with English abstract.
Clayton, R.N., O'Neil, J.R., Mayeda, T.K., 1972. Oxygen isotope exchange between quartz and water. J. Geophys. Res. B 77, 3057–3067.
Clayton, R.N., Mayeda, T.K., 1963. The use of bromine pentafluoride in the extraction of oxygen from oxides and silicates for isotopic analysis. Geochim. Cosmochim. Acta 27, 43–52.
Cox, S.F., Knackstedt, M.A., Braun, J., 2001. Principles of structural control on permeability and fluid hydrothermal system. SEG Rev. 14, 1–24.
Drummond, S.E., Ohmoto, H., 1985. Chemical evolution and mineral deposition in boiling hydrothermal systems. Econ. Geol. 80, 126–147.
Du, Y.S., Qin, X.L., Cao, Y., 2010. Sulfide and oxide inclusions in xenoliths and host rocks of Tongling area, Anhui Province. Miner. Deposits 71–84 in Chinese with English abstract.
Epstein, S., Sharp, R.P., Gow, A.J., 1965. Six-year record of oxygen and hydrogen isotope variations in South Pole firn. J. Geophys. Res. 70 (8), 1809–1814.
Friedman, I., 1953. Deuterium content of natural water and other substances. Geochim. Cosmochim. Acta 4, 89–103.
Gu, L.X., Chen, P.Y., Ni, P., Xu, Z.W., Xiao, J.X., Qiu, J.S., Zhang, Z.Z., Zhang, G.H., 2002. Comparative research on ore-forming fluids for the main types of hydrothermal copper-gold deposits in the Middle and Lower Reaches of the Yangtze River. J. Nanjing Univ. (Nat. Sci.) 38, 392–407 in Chinese with English abstract.
Gu, L.X., Zaw, K., Hu, W.X., Zhang, K.J., Ni, P., He, J.X., Xu, Y.T., Lu, J.J., Lin, C.M., 2007. Distinctive features of Late Paleozoic massive sulfide deposits in South China. Ore Geol. Rev. 31, 107–138.
Guo, W.M., Lu, J.J., Zhang, R.Q., Xu, Z.W., 2010. Ore textures and genetic significance of pyrrhotite from Dongguashan ore deposit in Tongling area, Anhui Province. Miner. Deposits. 29, 405–414 in Chinese with English abstract.
Guo, W.M., Lu, J.J., Zhang, R.Q., Zhao, Z.J., Xu, Z.W., 2011. The superimposed mineralization of the Dongguashan Cu deposit in Tongling Area, Anhui Province: evidence from the ore texture. Acta Geol. Sin. 85, 1223–1232 in Chinese with English abstract.
Hagemann, S.G., Luders, V., 2003. P-T-X conditions of hydrothermal fluid and precipitation mechanism of stibnite-gold mineralization at the Wiluna lode-gold deposit, Western Australia: conventional and infrared microthermometric constraints. Miner. Deposita. 38, 936–952.
Hall, D.L., Firedman, I., Bodnar, R.J., 1988. Freezing point depression of NaCl-KCl-H_2O solutions. Econ. Geol. 83, 197–202.
Hedenquist, J.W., Lowentern, J.B., 1994. The role of magma in the formation of hydrothermal lore deposits. Nature 370, 519–527.
Hou, Z.Q., Yang, Z.S., Lü, Q.T., Zeng, P.S., Xie, Y.L., Meng, Y.F., Tain, S.H., Xu, W.Y., Li,

H.Y., Jiang, Z.P., Wang, X.C., Yao, X.D., 2011. The large-scale Dongguashan deposit, Shizishan district in East China: carboniferous SEDEX-type massive sulfides overprinted by late Jurassic skarn Cu mineralization. Acta Geol. Sin. 5, 659–686 in Chinese with English abstract.

Hu, X.Z., Yang, Z.B., 2003. Ore-forming fluid characteristics and evolution process of the Qibaoshan Cu-polymetallic deposit in Liuyang, Hunan. Geol. Prospect. 39, 22–25 in Chinese with English abstract.

Jiang, S.Y., Ding, Q.F., Yang, S.Y., Zhu, Z.Y., Sun, M.Z., Sun, Y., Bian, L.Z., 2011. Discovery and significance of carbonate mud mounds from Cu-polymetallic deposits in the Middle and Lower Yangtze Metallogenic Belt: Examples from the Wushan and Dongguashan deposits. Acta Geol. Sin. 85, 744–756 in Chinese with English abstract.

Klemm, L.M., Pettke, T., Heinrich, C.A., 2008. Fluid and source magma evolution of the Questa porphyry Mo deposit, New Mexico, USA. Miner. Deposita 43, 533–552.

Li, Y., Li, J.W., Li, X.H., Selby, D., Huang, G.H., Chen, L.J., Zheng, K., 2017. An Early Cretaceous carbonate replacement origin for the Xinqiao stratabound massive sulfide deposit, Middle-Lower Yangtze Metallogenic Belt, China. Ore. Geol. Rev. 80, 985–1003.

Li, F.C., Liu, Y., Jin, Z.D., Geng, J.H., 1999. Role of fluid in the forming processes of ore deposits. Miner. Resour. Geol. 13, 129–134 in Chinese with English abstract.

Li, J.W., Pei, R.F., Zhang, D.Q., Mei, Y.X., Zang, W.S., Meng, G.X., Zeng, P.S., Li, T.J., Di, Y.J., 2007. Geochemical Characteristics of the Yanshanian Intermediate-acid Intrusive Rocks in the Tongling Mineralization Concentration Area, Anhui Province, and their geological implications. Acta Geosci. Sin. 28, 11–22 in Chinese with English abstract.

Li, Y., Selby, D., Li, X.H., Ottley, C.J., 2018. Multi-sourced metals enriched by magmatic-hydrothermal fluid in stratabound deposits of the Middle-Lower Yangtze River metallogenic belt, China. Geology 46 (5), 391–394. https://doi.org/10.1130./G39995.1.

Li, H.Y., Yang, Q.R., Li, Y.J., Hou, Z.Q., Yang, Z.S., Meng, Y.F., 2006. Geochemical characteristics of the Dongguashan copper deposit in Anhui Province. Acta Geosci. Sin. 27, 551–556 in Chinese with English abstract.

Li, H.Y., Ye, H.S., Wang, X.X., Yang, L., Wang, X.Y., 2014. Geology and ore fluid geochemistry of the Jinduicheng porphyry molybdenum deposit, East Qinling, China. J. Asian Earth. Sci. 79, 641–654.

Li, J.W., 2004. Ore-controlling structure of orefield and ore-forming chemical Kinetics of mineral assemblage area in Tongling. The Ph. D Dissertation of Chinese academy of Geological Sciences, Beijing, pp. 142 in Chinese with English abstract.

Lin, W.T., 1986. The influence of the temperature, pressure and chemical composition of the hydrothermal solution on the mineralization of the deposit. Anthol. Gold Silver Miner. 16, 18–34.

Ling, Q.C., Liu, C.Q., 2002. The characteristics of ore-forming fluid of Dongguashan stratabound skarn Cu deposit and its significance for deposit genesis. J. Jilin. Univ. (Earth Sci. Ed.) 32, 119–224 in Chinese with English abstract.

Ling, Q.C., Liu, C.Q., 2003. REE behavior during formation of strata-bound skarn and related deposit: a case study of Dongguashan skarn deposit in Anhui Province, China. Acta Petrol. Sin. 19, 192–200.

Liu, B., 2001. Density and isochoric formulae for NaC-H_2O inclusions with medium and high salinity and their applications. Geol. Rev. 47, 617–622 in Chinese with English abstract.

Liu, B., Duan, G.X., 1987. The density and isochoric formulae for NaCl-H_2O fluid inclusions (salinity $\leq$25 wt%) and their applications. Acta Mineral. Sin. 7, 345–352 in Chinese with English abstract.

Liu, W.C., Gao, D.Z., Chu, G.Z., 1996. In: Analysis of Tectonic Deformation and Metallogenic Prognosis in Tongling Area, Anhui Province. Geological Publishing House, Beijing, pp. 130 in Chinese.

Liu, J.H., Li, H., Xu, Z.W., Lu, X.C., Liu, S.M., Nie, G.P., 2009. Metallogenic geological settings and genesis of Dongguashan stratified cooper deposit. J. Geol. 3, 133–137 in Chinese with English abstract.

Liu, Z.F., Shao, Y.J., Zhang, Y., Wang, C., 2018. Geochemistry and geochronology of the Qingshanjiao granites: implications for genesis of the Dongguashan Cu-(Au) ore deposit in the Tongling ore district, Eastern China. Ore Geol. Rev. 99, 42–57.

Lu, H.Z., Fan, H.R., Ni, P., Ou, G.X., Shen, K., Zhang, W.H., 2004. In: Fluid Inclusion. Geological Publishing House, Beijing, pp. 490 in Chinese.

Lu, J.J., Guo, W.M., Chen, W.F., Jiang, S.Y., Li, J., Yan, X.R., Xu, Z.W., 2008. A metallogenic model for the Dongguashan Cu-Au deposit of Tongling, Anhui Province. Acta Petrol. Sin. 24, 1857–1864 in Chinese with English abstract.

Ma, X., Ge, H., 1989. Precambrian crustal evolution of eastern Asia. J. Asia Earth Sci. 3, 9–15.

Ma, Z.D., Shan, G.X., 1996. The background of regional lead isotopic compositions and its application in the Lower and Middle Reaches of the Yangtze River and Neighbouring areas. Acta. Acta Geosci. Sin. 4, 324–334 in Chinese with English abstract.

MaCrea, J.M., 1950. On isotope chemistry of carbonates and paleotemperature scale. J. Chem. Phys. 18, 849–857.

Mao, J.W., Wang, Y.T., Lehmann, B., Yu, J.J., Du, A.D., Mei, Y.X., Li, Y.F., Zang, W.S., Stein, H.J., Zhou, T.F., 2006. Molybdenite Re–Os and albite $^{40}Ar/^{39}Ar$ dating of Cu–Au–Mo and magnetite porphyry systems in the Changjiang valley and metallogenic implications. Ore Geol. Rev. 29, 307–324.

Mao, J.W., Shao, Y.J., Xie, G.Q., Zhang, J.D., Chen, Y.C., 2009. Mineral deposit model for porphyry-skarn polymetallic copper deposits in Tongling ore dense district of Middle-Lower Yangtze Valley metallogenic belt. Miner. Deposits 28, 209–219 in Chinese with English abstract.

Mao, J.W., Xie, G.Q., Duan, C., Pirajno, F., Ishiyama, D., Chen, Y.C., 2011. A tectono-genetic model for porphyry-skarn-stratabound Cu–Au-Mo–Fe and magnetite–apatite deposits along the Middle-Lower Yangtze River Valley, Eastern China. Ore Geol. Rev. 43, 294–314.

Ningwu Research Group, 1978. In: Magnetite Porphyry Deposits in Ningwu Area. Geological Publishing House, Beijing, pp. 196 in Chinese.

O'Neil, J.R., Clayton, R.N., Mayada, T.K., 1969. Oxygen isotope fractionation in divalent metal carbonates. J. Chem. Phys. 51, 5547–5558.

Ohmoto, H., 1972. Systematics of sulfur and carbon isotopes in hydrothermal ore deposits. Econ. Geol. 67, 551–578.

Ohmoto, H., 1986. Stable isotope geochemistry of ore deposits. Rev. Miner. 16, 491–559.

Ohmoto, H., Goldhaber, M.B., 1997. Sulfur and carbon isotopes. In: Barnes, H.L. (Ed.), Geochemistry of Hydrothermal Ore Deposits, third ed. Wiley, New York, pp. 435–486.

Pan, Y.M., Dong, P., 1999. The Lower Changjiang (Yangzi/Yangtze River) metallogenic belt, East China: intrusion- and wall rock-hosted Cu –Fe– Au, Mo, Zn, Pb, Ag deposits. Ore Geol. Rev. 15, 177–242.

Peng, S.L., Lai, J.Q., Mao, X.C., Shao, Y.J., Yang, M., Yang, B., 2012. In: Theories and Technologies for Large-scale Location and Quantification Prediction of Concealed Ore Bodies in the Depths of Crisis Mines. Geological Publishing House, Beijing, pp. 352 in Chinese.

Roedder, E., 1984. Fluid inclusions. Rev. Mineral. 12, 1–644.

Rui, Z.Y., Huang, C.K., Qi, G.M., Xu, Y., Zhang, H.T., 1984. In: Porphyry Copper (Molybdenum) Deposits of China. Geological Publishing House, Beijing, pp. 350 in Chinese.

Sheppard, S.M.F., 1986. Characterization and isotopic variations in natural waters. Rev. Mineral. 16 (1), 165–183.

Stacey, J.S., Hedlund, D.C., 1983. Lead-isotope compositions of diverse igneous rocks and ore deposits from southwestern New Mexico and their implications for early Proterozoic crustal evolution in the western United States. Geol. Soc. Am. Bull. 94, 43–57.

Tang, Y.C., Wu, C.Y., Chu, G.Z., Xing, F.M., Wang, Y.M., Cao, F.Y., Chang, Y.F., 1998. In: Geology of Copper–Gold Polymetallic Deposits in the along Changjiang Area of Anhui Province. Geological Publishing House, Beijing, pp. 351 in Chinese with English abstract.

Wang, X.C., Liu, L.G., Guo, X.Y., Zhou, Y.C., Wang, C.S., 2007. Regional SEDEX massive sulfide ore deposit. Geol. Anhui 17, 95–100 in Chinese with English abstract.

Wang, Q., Xu, J.F., Zhao, Z.H., Xiong, X.L., Bao, Z.W., 2003. Petrogenesis of the Mesozoic intrusive rocks in the Tongling area, Anhui Province, China and their constraint to geodynamic process. Sci. China (D) 33, 323–334 in Chinese.

Williams-Jones, A.E., Ferreira, D.R., 1989. Thermal metamorphism and H_2O-CO_2-NaCl immiscibility at Patapedia, Quebec: evidence from fluid inclusions. Contrib. Mineral. Petrol. 102, 247–254.

Wu, C.L., Chen, S.Y., Hao, M.Y., Shi, R.D., 2001. The origin and Features of the two intermediate-acid intrusive series in Tongling area, Anhui, China. Cont. Dyn. 6 (1), 1–12.

Wu, C.L., Gao, Q.M., Guo, H.P., Guo, X.Y., Liu, L.G., Cao, Y.H., Lei, M., Qing, H.P., 2010. Petrogenesis of the intermediate-acid intrusive rocks and zircon SHRIMP dating in Tongling Anhui, China. Acta Petrol. Sin. 26, 2630–2652 in Chinese with English abstract.

Wu, C.L., Guo, X.Y., Wang, C.S., Wu, X.P., Gao, Y.H., Lei, M., Qin, H.P., Liu, C.H., Li, M.Z., Chen, Q.L., 2013. Zircon U-Pb dating of high-K calc-alkaline intrusive rocks from Tongling: Implications for the tectonic setting. Geochimica 42, 11–28 in Chinese with English abstract.

Xie, Y.L., Hou, Z.Q., Yang, Z.M., Xu, W.Y., He, J.P., 2005. Evolution of multi-stage fluid and mineralization: Evidence from fluid inclusions in Yulong porphyry copper deposit, East Tibet. Acta. Petrol. Sin. 21, 1409–1415 in Chinese with English abstract.

Xie, J.C., 2008. In: The Diagenesis and Metallogenesis Research of MESOZOIC Magmatic Rocks in Tongling Region, Anhui Province. The Ph. D Dissertation of University of Science and Technology of China, Hefei, pp. 213 in Chinese with English abstract.

Xu, Z.W., Huang, S.S., Ni, P., Lu, X.C., Lu, J.J., Fang, C.Q., Hua, M., Jiang, S.Y., 2005. Characteristics and evolution of ore fluids in Dongguashan copper deposit, Anhui Province, China. Geol. Rev. 51, 36–41 in Chinese with English abstract.

Xu, Z.W., Lu, X.C., Gao, G., Fang, C.Q., Wang, Y.J., Yang, X.N., Jiang, S.Y., Chen, B.G., 2007. Isotope geochemistry and mineralization in the Dongguashan diplogenetic stratified copper deposit, Tongling area. Geol. Rev. 53, 44–51 in Chinese with English abstract.

Xu, X.C., Lu, S.M., Xie, Q.Q., Bai, L., Chu, G.Z., 2008b. SHRIMP Zircon U-Pb dating for the magmatic rocks in Shizishan ore-field of Tongling, Anhui Province, and its geological implication. Acta Geol. Sin. 82, 500–509 in Chinese with English abstract.

Xu, X.C., Lu, S.M., Xie, Q.Q., Lou, J.W., Chu, P.L., 2008a. Trace element geochemical characteristics of fluid inclusions of Anhui Province, and their geological implications. Acta Petrol. Sin. 8, 1865–1874 in Chinese with English abstract.

Xu, X.C., Yin, T., Lou, J.W., Lu, S.M., Xie, Q.Q., Zhu, P.L., 2010. Origin of Dongguashan stratabound Cu-Au skarn deposit in Tongling: Restraints of sulfur isotope. Acta Petrol. Sin. 26, 2739–2750 in Chinese with English abstract.

Xu, X.C., Lou, J.W., Xie, Q.Q., Xiao, Q.X., Liang, J.F., Zhu, P.L., 2011. Thermodynamic study of the paragenesis and fractionation of copper and gold in the Shizishan ore-field, Tongling, Anhui Province. Acta Geol. Sin. 85, 731–743 in Chinese with English abstract.

Xu, X.C., Bai, R.Y., Xie, Q.Q., Lou, J.W., Zhang, Z.Z., Liu, Q.N., Chen, L.W., 2012. Re-understanding of the geological and geochemical characteristics of the Mesozoic intrusive rocks from Tongling area of Anhui Province, and discussions on their genesis. Acta Petrol. Sin. 28, 3139–3169 in Chinese with English abstract.

Xu, X.C., Fan, Z.L., He, J., Liu, X., Liu, X.Y., Xie, Q.Q., Lu, S.M., Lou, J.W., 2014. Metallogenic model for the copper-gold-polymetallic deposits in Shizishan ore-field, Tongling, Anhui Province. Acta. Petrol. Sin. 30, 1054–1074 in Chinese with English abstract.

Xu, J.H., Xie, Y.L., Yang, Z.S., Meng, Y.F., Zeng, P.S., 2004b. Trace elements in fluid inclusions of submarine exhalation-sedimentation system in Tongling metallogenic province. Miner. Deposits 23, 344–352 in Chinese with English abstract.

Xu, W.Y., Yang, Z.S., Meng, Y.F., Zeng, P.S., Shi, D.N., Tian, S.H., Li, H.Y., 2004a. Genetic

model and dynamic migration of ore-forming fluids in carboniferous exhalation-sedimentary massive sulfide deposits of Tongling district, Anhui Province. Miner. Deposits 23, 353–364 in Chinese with English abstract.
Yan, J., Chen, J.F., Yu, G., Qian, H., Zhou, T.X., 2003. Pb lsotopic characteristics of Late Mesozoic mafic rocks from the Lower Yangtze Region: Evidence f or enriched mantle. Geol. J. China Univ. 2, 195–206 in Chinese with English abstract.
Yang, X.N., Xu, Z.W., Xu, X.S., Ling, H.F., Liu, S.M., Zhang, J., Li, H.Y., 2008. Zircon U-Pb geochronology and its implication for the temperature of Yanshanian magma in Tongling, Anhui Province. Acta. Geol. Sin. 62, 510–516 in Chinese with English abstract.
Yu, J.J., Mao, J.W., 2002. Distribution, geology and ore-forming environment of Kiruna-type iron deposits. Miner. Deposits 21, 83–86 Suppl. in Chinese.
Zartman, R., Doe, B., 1981. Plumbotectonics: the model. Tectonophysics 75, 135–162.
Zaw, K., Peters, S.G., Cromie, P., Burrett, C., Hou, Z.Q., 2007. Nature, diversity of deposit types and metallogenic relations of South China. Ore Geol. Rev. 31, 3–47.
Zeng, P.S., Pei, R.F., Hou, Z.Q., Meng, Y.F., Yang, Z.S., Tian, S.H., Xu, W.Y., Wang, X.C., 2005. The Dongguashan deposit in the Tongling mineralization cluster Area, Anhui: a large-sized superimposition type copper deposit. Acta Geol. Sin. 79, 106–131 in Chinese with English abstract.
Zhai, Y.S., Yao, S.Z., Lin, X.D., Zhou, X.N., Wan, T.F., Jin, F.Q., Zhou, Z.G., 1992. In: Fe-Cu-Au Metallogeny of the Middle-Lower Changjiang Region. Geological Publishing House, Beijing, pp. 235 in Chinese.
Zhai, Y.S., Xiong, Y.Y., Yao, S.Z., Liu, X.D., 1996. Metallogeny of copper and iron deposits in the Eastern Yangtze Craton, east–central China. Ore Geol. Rev. 11, 229–248.
Zhang, R.H., 1986. Sulfur isotopes and pyrite–anhydrite equilibria in a volcanic basin hydrothermal system of the Middle to Lower Yangtze River Valley. Econ. Geol. 81, 32–45.
Zhang, L.G., 1988. Lead isotopic compositions of feldspar and ore and their geologic significance. Miner. Deposits. 2, 55–64 in Chinese with English abstract.
Zhang, D.H., 1997. Geochemistry on boiling and mixing of fluids during the processes of hydrothermal deposits. Adv. Earth Sci. 12, 546–552 in Chinese with English abstract.
Zhang, W.H., Zhang, Z.J., Wu, G., 1996. Ore-forming fluid and mineralization mechanism. Earth Sci. Front. 3, 245–252 in Chinese with English abstract.
Zhou, T.F., Yue, S.C., Yuan, F., Zhai, Y., 2000. Two series of copper2gold deposits in the middle and lower reaches of the Yangtze River area (ML YRA) and the hydrogen, oxygen, sulfur and lead isotopes of their ore2forming hydrothermal systems. Sci. China D 43, 208–218.
Zhou, T.F., Fan, Y., Yuan, F., 2008. Advances on petrogenesis and metallogeny study of the mineralization belt of the Middle and Lower Reaches of the Yangtze River area. Acta Petrol. Sin. 24, 1665–1678 in Chinese with English abstract.
Zhou, T.F., Wang, S.W., Yuan, F., Fan, Y., Zhang, D.Y., White, N.C., 2016. Magmatism and related mineralization of the intracontinental porphyry deposits in the Middle-Lower Yangtze River Valley Metallogenic Belt. Acta Petrol. Sin. 32, 271–288 in Chinese with English abstract.
Zhu, B.Q., Li, X.H., Dai, D.M., 1998. In: System Theory and Application of Isotopes in the Earth Sciences: On the Chinese Mainland Crust-Mantle Evolution. Science Press, Beijing, pp. 330 in Chinese.